

ULTRAVIOLET THROUGH FAR-INFRARED SPATIALLY RESOLVED ANALYSIS OF THE RECENT STAR FORMATION IN M81 (NGC3031)

PABLO G. PÉREZ-GONZÁLEZ¹, ROBERT C. KENNICUTT JR.¹, KARL D. GORDON¹, KARL A. MISSELT¹, ARMANDO GIL DE PAZ^{2,3}, CHARLES W. ENGELBRACHT¹, GEORGE H. RIEKE¹, GEORGE J. BENDO^{4,1}, LUCIANA BIANCHI⁵, SAMUEL BOISSIER^{6,3}, DANIELA CALZETTI⁷, DANIEL A. DALE⁸, BRUCE T. DRAINE⁹, THOMAS H. JARRETT¹⁰, DAVID HOLLENBACH¹¹, MOIRE K. M. PRESCOTT¹

Last edited: July 7, 2018

ABSTRACT

The recent star formation (SF) in the early-type spiral galaxy M81 is characterized using imaging observations from the far-ultraviolet (UV) to the far-infrared (IR). We compare these data with models of the stellar, gas, and dust emission for sub-galactic regions. Our results suggest the existence of a diffuse dust emission not directly linked to the recent SF. We find a radial decrease of the dust temperature and dust mass density, and in the attenuation of the stellar light. The IR emission in M81 can be modeled with three components: 1) cold dust with a temperature $< T_c > = 18 \pm 2$ K, concentrated near the HII regions but also presenting a diffuse distribution; 2) warm dust with $< T_w > = 53 \pm 7$ K, directly linked with the HII regions; and 3) aromatic molecules, with diffuse morphology peaking around the HII regions. We derive several relationships to obtain total IR luminosities from IR monochromatic fluxes, and we compare five different star formation rate (SFR) estimators for HII regions in M81 and M51: the UV, H α , and three estimators based on *Spitzer* data. We find that the H α luminosity absorbed by dust correlates tightly with the 24 μ m emission. The correlation with the total IR luminosity is not as good. Important variations from galaxy to galaxy are found when estimating the total SFR with the 24 μ m or the total IR emission alone. The most reliable estimations of the total SFRs are obtained by combining the H α emission (or the UV) and an IR luminosity (especially the 24 μ m emission), which probe the unobscured and obscured SF, respectively. For the entire M81 galaxy, about 50% of the total SF is obscured by dust. The percentage of obscured SF ranges from 60% in the inner regions of the galaxy to 30% in the outer zones.

Subject headings: dust, extinction — galaxies: individual (M81, NGC3031) — galaxies: photometry — galaxies: ISM — galaxies: spiral — galaxies: stellar content — infrared: galaxies

1. INTRODUCTION

The multiwavelength analysis of the stellar populations in nearby galaxies is one of the most powerful ways of understanding how galaxies form and evolve (see, e.g., Meurer et al. 1999; Conselice et al. 2000; Calzetti 2001; Pérez-González et al. 2003a,d; Brinchmann et al. 2004). Indeed, relatively bright and close objects are the best laboratories to study galaxy evolution, given that we can obtain high quality data over a wide range of wavelengths with incomparable depth and physical resolution. The detailed characterization of nearby galaxies is essential

to establish the benchmark to which analysis of galaxies at intermediate and high redshift must refer.

The multiwavelength data can be used to relate the scale where star formation normally occurs (i.e., the typical size of an HII region, 20-200 pc; see, e.g., Youngblood & Hunter 1999) to the scales of the dynamical structures (bulge, arms, bars) and the entire galaxy (i.e., several kpc). Moreover, the combination of data from the ultraviolet (UV) to the far-infrared (FIR) and radio also allows simultaneous analysis of the three main (emitting) components of a galaxy: the stars, the dust, and the gas.

One of the main problems in the study of the stellar populations in unresolved galaxies is the determination of the dust attenuation of the stellar emission. Indeed, the correction for dust extinction is the main source of uncertainty in the estimation of important characteristics of entire galaxies (i.e., of integrated stellar populations), such as the star formation rate (SFR), age or metallicity (Kennicutt 1998; Gordon et al. 2000; Calzetti 2001; Bell 2002). This problem is even more severe when studying galaxies with current star formation, given that this process occurs in zones where the gas and dust densities are high (and the higher the densities, the more intense the star formation), resulting in high extinctions with large spatial variations. This effect translates into significant uncertainties concerning the evolution of galaxies throughout the Hubble time (see Hopkins 2004, and ref-

¹ The University of Arizona, Steward Observatory, 933 N Cherry Avenue, Tucson, AZ 85721

² Departamento de Astrofísica, Facultad de CC. Físicas, Universidad Complutense de Madrid, E-28040 Madrid, Spain

³ Observatories of the Carnegie Institution of Washington, 813 Santa Barbara Street, Pasadena, CA 91101

⁴ Blackett Laboratory, Imperial College, London SW7 2AZ, UK

⁵ Department of Physics and Astronomy, Johns Hopkins University, 3400 North Charles Street, Baltimore, MD 21218

⁶ Laboratoire d'Astrophysique de Marseille, Traverse du Siphon-Les trois Lucs, BP8-13376 Marseille Cedex 12, France

⁷ Space Telescope Science Institute, 3700 San Martin Drive, Baltimore, MD 21218

⁸ Department of Physics and Astronomy, University of Wyoming, Laramie, WY 82071

⁹ Princeton University Observatory, Peyton Hall, Princeton, NJ 08544

¹⁰ Spitzer Science Center, California Institute of Technology, 100-22 IPAC, Pasadena, CA 91125

¹¹ NASA Ames Research Center, Moffett Field, CA 94035

erences therein).

One way to overcome the problem of dust attenuation is to combine data covering the widest wavelength range possible. This range must include the UV, where the emission comes mainly from hot young massive stars, and the optical and near-infrared, which are normally dominated by more evolved low mass stars. Spectroscopic observations and narrow-band imaging concentrating on emission-lines are also useful to study the stellar populations (for example, the H α emission is directly linked to the youngest stars). Much work characterizing the stellar populations in galaxies using a variety of such datasets and technical approaches has appeared in the literature (among others, Bell & de Jong 2001; Papovich et al. 2001; Pérez-González et al. 2003c; Kauffmann et al. 2003; Heavens et al. 2004).

A complementary way to study the star formation (especially the most recent) in galaxies is using mid- and far-infrared observations. The emission at these wavelengths comes mainly from dust heated by stellar light (see, e.g., Walterbos & Greenawalt 1996; Kennicutt 1998; Devriendt et al. 1999). The total IR emission (integrated from 8 to 1000 μm) has been claimed to be an optimum SFR tracer for entire galaxies (at least for the ones dominated by star formation and with high dust content), given that it is not affected by dust attenuation (see Sauvage & Thuan 1992; Sanders & Mirabel 1996; Kennicutt 1998, and references therein). The IR has been widely used for studying local and distant star-forming galaxies (e.g., Rieke & Low 1972; Saunders et al. 1990; Flores et al. 1999; Meurer et al. 1999; Franceschini et al. 2001; Rowan-Robinson 2001; Chary & Elbaz 2001; Kewley et al. 2002; Goldader et al. 2002; Dale & Helou 2002; Pérez-González et al. 2005). Although it is generally assumed that the heating of the dust emitting in the IR is dominated by light coming from the young hot stars (which would mean that the IR is a robust SFR estimator), it remains unclear how much the older stellar populations contribute (i.e., how we should correct the integrated IR emission to obtain robust values of the current SFR). Moreover, the validity of the equations correlating the SFR and the IR emission, which were derived for entire galaxies, is not well established when working at sub-galactic scales (for example, with HII regions). Finally, another interesting topic under study is the role of the aromatic molecules (loosely termed polycyclic aromatic hydrocarbons, PAHs) in the star formation event (see Leger & Puget 1984, Allamandola et al. 1985, Puget & Leger 1989; and most recently, Förster Schreiber et al. 2004; Boselli et al. 2004; Peeters et al. 2004).

The study of the stellar populations in galaxies, and more specifically of the most recent star formation, has experienced remarkable progress in the past few years, as we have been able to gather observations from the UV to the FIR with similar depths and spatial resolutions. Two space missions have contributed significantly to this observational advance: the Galaxy Evolution Explorer (GALEX; Martin et al. 2005) and the *Spitzer* Space Telescope (Werner et al. 2004a), which have unprecedented sensitivity and angular resolution and coverage in the UV and IR, respectively. These facilities, jointly with other ground-based and space telescopes, are being used by the *Spitzer* Infrared Nearby Galaxy Sur-

vey (SINGS, Kennicutt et al. 2003) to collect very high quality data from the UV to the FIR for a large sample of nearby resolved galaxies representative of the local galaxy population. The main goal of SINGS is to provide a complete multiwavelength dataset to understand the formation of stars in galaxies and the properties of the dust. The SINGS dataset, including up to 7 broad-band measurements in the IR, and extensive ancillary data at optical and radio wavelengths, has proved to be very useful for exploring these topics (see, e.g., Dale et al. 2005; Calzetti et al. 2005).

In this paper, our main goal is to study the characteristics of the most recent star formation in a galaxy, testing the IR emission as a SFR estimator for sub-galactic regions by empirically analyzing its correlation with the “classical” star formation tracers, the UV continuum and the ionized hydrogen emission-lines (in our case, the H α emission). This paper complements a similar analysis of M51 by Calzetti et al. (2005). Combining the data for the three SFR estimators, we can account for: 1) the photons coming from the newly-formed stars which do not interact with anything or are just scattered, and we detect in the UV; 2) the photons that interact with the gas, and are reemitted in emission lines; and 3) the photons that interact with the dust, and are reemitted in the IR. By checking the consistency among these indicators, a clearer picture of the star formation event is obtained. The results in this paper will be used to study the different stellar populations (i.e., the star formation history) of M81 in a future work (Pérez-González et al. 2006, in preparation).

This work concentrates on one of the galaxies in the SINGS sample, M81 (NGC3031), the largest in angular extent in the survey (with a size of $27' \times 14'$). M81 is a face-on spiral [SA(s)ab type, de Vaucouleurs et al. 1992] at a distance of 3.63 ± 0.34 Mpc (Freedman et al. 1994; Karachentsev et al. 2002). At this distance, the resolution of the MIPS images corresponds to 100-700 pc (depending on the channel). This resolution allows the study of the star formation in M81 at different scales ranging from typical sizes of HII regions to the size of large star-forming complexes and dynamical structures (bulge, arms). M81 is an object with moderate global star formation ($SFR = 0.4 - 0.8 M_{\odot} \text{yr}^{-1}$; Devereux et al. 1995, Lin et al. 2003, Gordon et al. 2004) and extinction ($A(V) = 0.5 - 1.0$, Garnett & Shields 1987, Kong et al. 2000). It forms part of a group of about 25 galaxies with clear interactions among them (for example, among M81, M82, and NGC3077; see Solinger et al. 1977). M81 also harbors an active galactic nucleus (Peimbert & Torres-Peimbert 1981; Filippenko & Sargent 1988) classified as a LINER Sy1.5-1.8 (Heckman 1980; Shuder & Osterbrock 1981; Ho et al. 1997). The nucleus is a strong x-ray (Elvis & van Speybroeck 1982; Fabbiano 1988; Petre et al. 1993; Page et al. 2003; La Parola et al. 2004) and UV (Wu et al. 1980; Hill et al. 1992; Reichen et al. 1994) emitter. M81 has been extensively studied at all wavelengths from x-rays to the radio. In this work, we will make use of the UV and emission-line data published for some of the individual HII regions in M81 (Garnett & Shields 1987; Kaufman et al. 1987; Hill et al. 1995; Lin et al. 2003), jointly with the new *Spitzer* and GALEX data.

This paper is organized as follows. Section 2 describes the data compiled for this work. In Section 3, we present the models of the stellar and dust thermal emission developed to analyze the UV-to-FIR data of M81. In Section 4, we discuss the contribution of stellar light to the mid-IR fluxes, and different ways to estimate the total IR luminosity from monochromatic fluxes measured by *Spitzer*. We also concentrate on the analysis of the dust properties in several sub-galactic regions in M81. Section 5 compares different SFR estimators for selected HII regions. Section 6 summarizes our conclusions.

2. THE DATA

We have compiled a variety of imaging and spectroscopic data for M81 covering the ultraviolet (UV), optical, near-IR (NIR), mid-IR (MIR), and far-IR (FIR) wavelengths. The sources for each piece of the dataset are described in the following subsections.

2.1. The *Spitzer* data

Observations of M81 in the MIR and FIR were carried out with *Spitzer* (Werner et al. 2004a) as a part of the SINGS Legacy Project (Kennicutt et al. 2003). The Infrared Array Camera (IRAC, Fazio et al. 2004) obtained images of M81 at 3.6, 4.5, 5.8, and 8.0 μm in May 2004. The data were processed with version S10.0.3 of the Spitzer Science Center pipeline, and then mosaicked to produce a single image for each channel with a scale of 0.76 arcsec pixel⁻¹ (Regan et al. 2004). The Full Width at Half Maximum (FWHM) of the Point Spread Function (PSF) is 1.7'', 1.7'', 1.9'', and 2.0'' for the 3.6, 4.5, 5.8, and 8.0 μm channels, respectively (corresponding to a physical size of $\sim 30\text{-}35$ pc at the distance of M81). The IRAC images were calibrated using the factors and aperture corrections (to properly measure the photometry of extended sources) found in Reach et al. (2005). These corrections range from 6% in channel 1 to 26% in channel 4. The 1- σ sensitivities of the images are [0.2, 2.2, 2.0, 1.9] $\mu\text{Jy arcsec}^{-2}$ at [3.6, 4.5, 5.8, 8.0] μm ([25.7, 23.0, 23.2, 23.2] mag(AB) arcsec⁻²).

Images at 24, 70 and 160 μm were taken with the Multiband Imaging Photometer for *Spitzer* (MIPS, Rieke et al. 2004) at three different epochs (to remove artifacts) in November 2003 and October 2004. The three epochs were processed and mosaicked together using the DAT reduction pipeline (Gordon et al. 2005), producing final mosaics with pixel scales half of the original values (1.25, 4.9, and 8 arcsec pixel⁻¹ for 24, 70, and 160 μm , respectively). These mosaics have a size of $1^\circ \times 2.5^\circ$, large enough to include the entire galaxy. The FWHM of the PSFs are 5.7'', 16'', 38'' for the 24, 70, and 160 μm channels (corresponding to 100, 282, and 669 pc in M81). The 1- σ sensitivities of the images are [0.9, 7.0, 20.0] $\mu\text{Jy arcsec}^{-2}$ at [24, 70, 160] μm ([24.0, 21.8, 20.7] mag(AB) arcsec⁻²).

2.2. The *GALEX* data

The Galaxy Evolution Explorer (*GALEX*) observed M81 on December 8th 2003 for a total of 3089 seconds split across two orbits. Note that since *GALEX* only observes during night-time the usable time per orbit is only ~ 1700 seconds. Images in the two *GALEX* bands, far-ultraviolet (FUV; $\lambda_{\text{eff}}=151.6$ nm) and near-ultraviolet

(NUV; $\lambda_{\text{eff}}=226.7$ nm), were obtained simultaneously. The UV light is separated in these two bands by a dichroic beam splitter that also acts as a field-aberration corrector. Individual UV photons are then detected using micro-channel plates with crossed delay-line anodes. The photon lists created are processed by the *GALEX* pipeline to produce the corresponding intensity maps in counts per second with a final scale of 1.5 arcsec pixel⁻¹ (see Morrissey et al. 2005). The reader is referred to Martin et al. (2005) for a more detailed description of the *GALEX* mission.

The large field of view of the *GALEX* instrument (a circle of 1.2° in diameter) allowed it to cover the entire M81 galaxy, along with M82 and Holmberg IX, in one single pointing. The absolute flux calibration of the *GALEX* data is based on multiple observations of white dwarf standard stars. Zero-point errors are estimated to be of the order of 0.15 mag both in the FUV and NUV channels. The astrometry of the *GALEX* images is based on the Tycho-2 catalog (Høg et al. 2000) and it is found to have a RMS error less than 1 pixel. The FWHM of the PSF of the *GALEX* images is a function of the brightness of the source and the position on the detector. In the case of the observations of M81 the FWHM is approximately 5'' and 6'' (88 and 106 pc at the M81 distance, respectively), respectively for the FUV and NUV bands. The 1- σ sensitivities of the images of M81 are [1.8, 1.7] $\times 10^{-2}$ $\mu\text{Jy arcsec}^{-2}$ ([28.3, 28.3] mag(AB) arcsec⁻²) for the FUV and NUV channels, respectively.

2.3. Optical and near-infrared data

We complement the UV *GALEX* data and the MIR/FIR *Spitzer* images with optical and NIR data obtained at different ground-based facilities. *UBVRI* observations were carried out in 2004-2005 with the 2.3m Bok Telescope at Steward Observatory using the prime focus wide-field imager (Williams et al. 2004). Standard reduction algorithms for CCD images were applied to the data. We took special care with the distortion correction of the large $1^\circ \times 1^\circ$ images. The depths of these optical images are [7.1, 7.5, 11.0, 12.0, 2.6] $\times 10^{-2}$ $\mu\text{Jy arcsec}^{-2}$ ([26.8, 26.7, 26.3, 26.2, 27.9] mag(AB) arcsec⁻²) for the *UBVRI* bands (1- σ sensitivity), respectively.

NIR images (*JHK_s* bands) were taken from the Two Micron All Sky Survey (2MASS; Jarrett et al. 2000). The depths are [80, 140, 140] $\mu\text{Jy arcsec}^{-2}$ ([19.1, 18.5, 18.5] mag(AB) arcsec⁻²) in *JHK* (1- σ sensitivity), respectively.

Finally, we have used the narrow-band H α image taken from Greenawalt et al. (1998). The calibration of this image was carried out by measuring the H α +*[NII]* fluxes for all the HII regions cataloged in Kaufman et al. (1987) and Lin et al. (2003). Our calibration gives a total H α +*[NII]* flux for M81 of 4.7 ± 1.0 erg s⁻¹ cm⁻². The difference between this flux and the estimations of Greenawalt et al. (1998, 4.8 ± 0.7 erg s⁻¹ cm⁻²) and Devereux et al. (1995, 4.53 ± 1.35 erg s⁻¹ cm⁻²) is less than 4% and well within errors. In the following discussion, we will use pure H α fluxes that have been measured from the narrow-band image and corrected for *[NII]* contamination assuming an average *[NII]*/H α ratio of 0.4 (Garnett & Shields 1987). The 1- σ H α sensitivity limit of this image is 1×10^{-17} erg s⁻¹ cm⁻² arcsec⁻².

2.4. Photometry

We produced two sets of images, one set composed of images convolved to match the PSF of the image in our dataset with the worst resolution, the MIPS 160 μm image, and another set convolved to the MIPS 24 μm PSF, which is adequate to study the dust emission in individual HII regions. The World Coordinate System (WCS) for the UV, optical, NIR, and IRAC images was determined using 2MASS stars (more than 30 per frame). For the MIPS images, given that stars are normally very faint or undetected, we determined the WCS by using bright point-like regions detected in the IRAC bands. The images were aligned and cropped to the same size using the WCS for each frame.

For the image set convolved to the 160 μm resolution (160RES set hereafter), we selected 49 circular regions in the arms corresponding to resolved peaks in the 160 μm emission. We also selected 6 regions in the zone between the arms and the nucleus dominated by a more diffuse emission, two regions around the nucleus (one enclosing the inner nucleus, and another the circumnuclear region), and an aperture enclosing the entire galaxy. The radii of the photometric apertures were chosen to enclose most of the emission from the peaks (ranging from 0.6 to 1.8 kpc). The photometric apertures are shown in the left panel of Figure 1. Most of the selected regions were identified in the 24 μm and $\text{H}\alpha$ images with bright star-forming complexes, normally enclosing several individual HII regions (see right panel of Figure 1).

Proper background subtraction is essential when dealing with data spanning a wide range of wavelengths, especially if some of the images include very bright diffuse emission (such as the images of M81 in the MIR and FIR, see Gordon et al. 2004). We followed two approaches in the background estimation, each of them optimized for one of the two problems that we can address with this dataset. First, analyzing the properties of the global stellar population and the dust in several sub-galactic regions in M81 requires photometry that accounts for the entire emission of the region at any wavelength (including all stars, gas and dust in the region), so the best approach is to estimate a global background, i.e., a background that only includes the sky emission around the galaxy. However, second, for studying different SFR estimators, one of the main goals of this paper, it is important to account for the diffuse emission surrounding each star-forming complex. This emission is probably not directly related to the recent star formation, but arises from a source in the galaxy of a different origin (e.g., older stars, diffuse dust emission).

As an example, the 160 μm image of M81 shows a bright diffuse component that is not linked with any star-forming region (detected in the $\text{H}\alpha$ or 24 μm image). Other authors have also detected an extended and diffuse dust component beyond the star-forming disk in a variety of galaxies (see, among others, Hippelein et al. 2003; Popescu & Tuffs 2003; Hinz et al. 2004; Stickel et al. 2005; Popescu et al. 2005). The cold dust responsible for this emission is probably not (only) heated by the newly-formed stars, but by a more diffuse heating source, such as an evolved stellar population or $\text{Ly}\alpha$ and Lyman continuum photons escaping from HII regions (see Popescu et al. 2005).

The global background for M81 was measured in several zones located around the galaxy, which were observed at all wavelengths and clear of bright objects (green rectangles and elliptical annulus in the left panel of Figure 1). The local background was measured in small circular apertures around the arms (green circles in the left panel of Figure 1). For each individual region studied, we averaged the values obtained for the two closest sky apertures, one in the inter-arm region and another in the outer part of the arm. Two photometric catalogs were produced using the two background estimations (marked as LOCALBKG and GLOBALBKG photometry), and the implications of each choice are discussed in the following Sections.

For the image set convolved to the 24 μm resolution (24RES hereafter), we extracted photometry for 59 individual HII regions found in Garnett & Shields (1987) and Kaufman et al. (1987). These regions are shown in the right panel of Figure 1. The original aperture sizes used by those authors were very small compared with the resolution of our 24 μm image, so we extracted photometry for circular apertures with a 7 pixels ($\sim 8.4''$) radius, which enclosed most of the emission for each HII region as seen in the $\text{H}\alpha$ image (the radius of these apertures corresponds to 0.1 kpc), and is an adequate match to the 24 μm PSF. The sky estimation was performed locally in circular apertures near the individual HII regions¹² (green circles in the right panel of Figure 1). For the entire galaxy, the sky was measured in an elliptical annulus.

Aperture corrections were applied to the fluxes of the regions selected in each image set to obtain the photometry for an “infinite aperture” using theoretical STinyTim PSFs for the MIPS bands. All the fluxes were corrected for Galactic extinction using a value of $A(B) = 0.346$ (Schlegel et al. 1998) and the extinction law published by Cardelli et al. (1989) with $R_V = 3.1$. The fluxes for all regions are given in Tables 1 and 2.

3. MODELS OF THE UV-TO-FIR EMISSION OF M81

3.1. The stellar and gas emission model

For the regions selected in the 160RES image set, we built spectral energy distributions (SEDs) from 0.150 μm to 160 μm . SEDs were also built for the HII regions selected in the 24RES image set from 0.150 μm to 24 μm . We then fitted the SEDs with models of the stellar, gas, and dust emission. These models will be used in this paper to remove the stellar contribution to the emission in the MIR and FIR bands. In a future paper, the results on the stellar populations of M81 obtained with these models will be discussed in detail.

The photometric points at wavelengths bluer than 4.5 μm were fitted to stellar population synthesis models. We also included the $\text{H}\alpha$ equivalent width in the fits (see Gil de Paz et al. 2000; Pérez-González et al. 2003b,c).

We assumed that the star formation history in each region can be described by a burst with an exponentially declining star formation rate with time scale τ ,

¹² Only one approach of the background determination was followed for the 24RES case (local background), given that we were interested in comparing the SFR estimators. This task benefits from a proper subtraction of the diffuse emission surrounding the HII regions.

TABLE 1
POSITIONS AND PHOTOMETRY (GLOBALBKG AND LOCALBKG CASES) FOR THE REGIONS SELECTED AT 160 μM RESOLUTION.

Field	BKG	M81	Reg02	Reg03	Reg04	Reg05	Reg06	Reg07	Reg08	Reg09
RA (J2000)		09:55:32.2	09:55:32.2	09:55:32.2	09:55:16.7	09:55:05.0	09:55:35.1	09:55:53.3	09:55:35.7	09:55:26.4
DEC (J2000)		69:03:59.0	69:03:59.0	69:03:59.0	69:06:12.4	69:05:22.9	69:06:24.1	69:01:47.0	69:07:29.6	69:08:08.9
radius		680.0	64.0	104.0	40.9	50.8	51.3	56.0	31.9	31.6
$\log [L(H\alpha)]$	G	40.78	39.67	39.40	38.79	38.88	39.10	38.86	39.10	39.24
	L	40.69	39.53	39.18	38.40	38.42	38.82	38.54	39.06	39.09
$\log [L(3.6)]$	G	43.18	42.63	42.38	41.63	41.62	41.75	41.81	41.14	41.10
	L
$\log [L(4.5)]$	G	42.84	42.28	42.03	41.27	41.25	41.40	41.49	40.81	40.77
	L
$\log [L(5.8)]$	G	42.63	41.98	41.76	41.05	41.06	41.21	41.21	40.73	40.72
	L	41.42	39.30	40.03	...	40.32	40.22
$\log [L(8.0)]$	G	42.61	41.76	41.58	40.93	40.99	41.18	41.11	40.88	40.88
	L	42.33	40.65	40.79	40.34	40.42	40.78	40.58	41.05	40.70
$\log [L(24)]$	G	41.98	41.25	40.90	40.20	40.29	40.49	40.38	40.28	40.35
	L	41.92	41.13	40.68	39.90	39.96	40.31	40.20	40.27	40.28
$\log [L(70)]$	G	42.67	41.83	41.62	40.98	41.00	41.23	41.15	40.98	41.05
	L	42.68	41.79	41.52	40.79	40.72	41.11	41.08	40.98	41.00
$\log [L(160)]$	G	42.99	41.78	41.78	41.27	41.37	41.55	41.46	41.30	41.31
	L	42.99	41.67	41.62	41.05	41.11	41.38	41.36	41.29	41.22

NOTE. — Table 1 is available in its entirety via the link to the machine-readable version above. Units of right ascension are hours, minutes, and seconds, and units of declination are degrees, arcminutes, and arcseconds. The radius of each region is given in arcsec. All luminosities refer to observed values (no internal or Galactic extinction corrections have been applied) and the units are erg s^{-1} . The first row for each wavelength refers to the photometry measured with a GLOBALBKG estimation (second column set to the value G), and the second to the LOCALBKG case (second column set to the value L).

TABLE 2
POSITIONS AND PHOTOMETRY FOR THE REGIONS SELECTED AT 24 μM RESOLUTION.

Field	M81	kauf240	kauf104	kauf101	Munch1	kauf102	kauf198	No17	kauf197
RA (J2000)	09:55:33.2	09:56:27.0	09:56:20.6	09:56:19.9	09:56:18.9	09:56:18.3	09:56:17.2	09:56:17.2	09:56:16.6
DEC (J2000)	69:03:55.1	69:04:24.0	69:01:12.1	69:04:25.3	68:49:40.9	69:03:34.9	69:06:07.4	69:06:07.4	69:05:36.2
radius	680.0	8.4	8.4	8.4	8.4	8.4	8.4	8.4	8.4
$A(V)$...	1.05	1.31	1.01	0.37	1.91	0.42	1.60	0.67
$\log [L(FUV)]$	42.74	39.49	39.67	40.00	39.51	39.98	40.22	40.22	39.88
$\log [L(NUV)]$	42.82	39.25	39.57	39.93	39.06	39.83	40.08	40.08	39.84
$\log [L(H\alpha)]$	40.77	37.79	38.14	38.24	38.01	38.41	38.38	38.38	38.28
$\log [L(8.0)]$	42.61	39.08	39.64	39.46	38.50	39.65	39.64	39.64	39.64
$\log [L(24)]$	41.99	38.73	39.73	39.00	38.67	39.35	39.37	39.37	39.42

NOTE. — Table 2 is available in its entirety via the link to the machine-readable version above. Units of right ascension are hours, minutes, and seconds, and units of declination are degrees, arcminutes, and arcseconds. The radius of each region is given in arcsec. All luminosities refer to observed values (no internal or Galactic extinction corrections have been applied) and the units are erg s^{-1} .

metallicity Z , age t , and attenuated by an amount described by the quantity $A(V)$. The attenuation at any wavelength was calculated from the free parameter $A(V)$ using the Charlot & Fall (2000) recipe. The stellar emission in our models was taken from the PEGASE code (Fioc & Rocca-Volmerange 1997), and we added the emission from the gas heated by the stars (emission lines and nebular continuum) using the emission and recombination coefficients given by Ferland (1980) for an electron temperature $T_e = 10^4 \text{ K}$, the relations given by Brocklehurst (1971), and the theoretical line-ratios expected for a low density gas ($n_e = 10^2 \text{ cm}^{-3}$) with $T_e = 10^4 \text{ K}$ in the recombination Case B (Osterbrock 1989). We fixed the metallicity of our models to Z_\odot , based on the results from Zaritsky et al. (1994), Stauffer & Bothun (1984), and Kong et al. (2000), who showed that the metallicity in M81 is nearly solar with a very weak radial dependence. We probed the solution

space in the following ranges for the three remaining free parameters $[\tau, t, A(V)]$: 1) we assumed τ values from an almost instantaneous burst ($\tau = 1 \text{ Myr}$) to an almost constant SFR ($\tau = 15 \text{ Gyr}$) using a logarithmic interval of 0.1dex (in yr); 2) ages were probed from $t = 1 \text{ Myr}$ to $t = 13 \text{ Gyr}$ in logarithm intervals; 3) extinction values ranged from $A(V) = 0$ to $A(V) = 3$ in intervals of 0.05 mag.

3.2. The model of emission by dust

After fitting the UV-to-NIR part of the SEDs with stellar/gas emission models, we subtracted the contribution from the stars/gas to the fluxes in the MIR and FIR. We then fitted models of dust emission to the remaining fluxes. These models are described by an equation of the form:

$$F_{\text{dust}}(\lambda) = \sum C^i \kappa^i(\lambda) B_\lambda(T_{\text{dust}}^i) \quad (1)$$

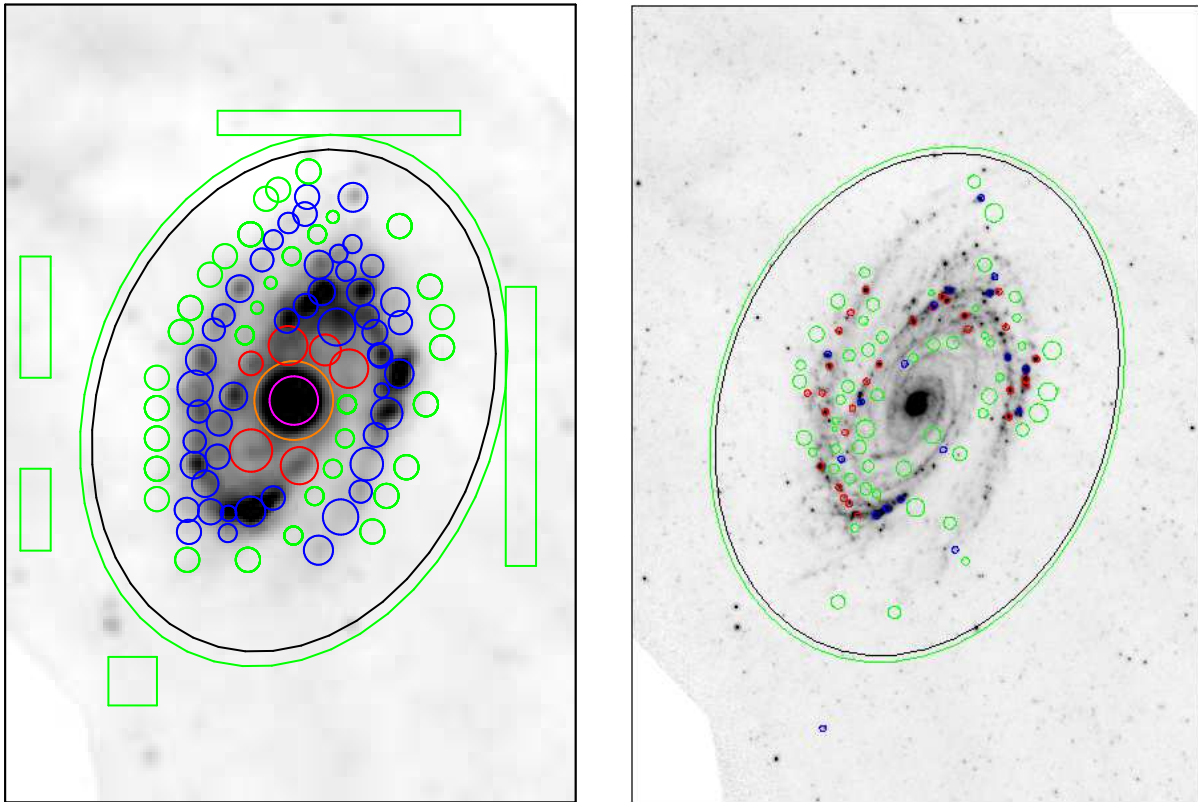


FIG. 1.— The regions for which we extracted photometry from M81 are shown superimposed on the MIPS 24 μm image. The left panel shows the effect of convolving to the 160 μm resolution, and the right panel show the photometric apertures for the HII regions selected at the original 24 μm resolution. On the left panel, blue circles enclose star-forming complexes in the arms. The red circles enclose regions of diffuse emission in the zone between the nucleus and the arms. The magenta region encloses the inner nucleus of M81. The area outside the magenta circle and inside the orange circles is defined as the circumnuclear region. Green rectangles show the zones used for estimating the global background (selected to be free of bright sources in all the images). For the right panel, blue regions come from the sample of HII regions studied by Garnett & Shields (1987), and red regions were found in Kaufman et al. (1987). For both panels, the black ellipse depicts the aperture used for the entire M81 galaxy. The green ellipse and circles show the zones where the local sky was measured (see text for details).

where the sum extends over the number of dust components (each of them emitting as a modified blackbody), $C_i = M_{\text{dust}}^i / D^2$, D is the luminosity distance to the source, M_{dust}^i are the masses of each dust component, and κ_i are the wavelength dependent mass absorption coefficients. We adopted a model with 3 components: 1) warm silicates; 2) cold silicates (both components with grains of sizes $a \sim 0.1 \mu\text{m}$); and 3) aromatic molecules. Mass absorption coefficients for astronomical silicates were computed from Mie theory using the dielectric functions of Laor & Draine (1993). Cross sections for the aromatic molecules were taken from Li & Draine (2001). As the canonical aromatic spectrum (see, e.g., Werner et al. 2004b) exhibits no features beyond 20 μm , we re-computed the aromatic cross-sections (and mass absorption coefficients) leaving off the last three terms of Equation 11 in Li & Draine (2001). The aromatic component is included mainly for completeness. The aromatic emission is a stochastic process rather than an equilibrium process as assumed in Equation 1. This means that our model should underestimate the total aromatic masses. A proper treatment of the stochastic aromatic emission would require a full radiative transfer solution to derive the radiation field at each position in the galaxy. The attendant assumptions are beyond the

scope of this paper, but will be addressed in forthcoming detailed models of individual regions. Our results are not affected by this issue, given that they only refer to the total dust masses, to which aromatic molecules make only a minor contribution.

The fitting procedure is based on a Monte-Carlo technique. With our assumptions about the components in the observed SED, we searched a limited set of parameters for dust mass (through C_i) and temperature for each component. We assumed temperature ranges of 200–750 K, 35–100 K, and 10–25 K for the aromatics, warm, and cold silicates, respectively. At each set of temperature points, a similar grid of mass scalings (C_i) was explored for each component. After an initial, coarse grid search, a finer temperature and mass scaling grid was defined for each component and the procedure repeated. We iterated this procedure (typically only two refinements of the grid were needed) until a good fit was found based on a χ^2 goodness of the fit estimator. While the results of this technique are not unique, it yields representative estimates of both the dust mass and temperature (and errors obtained through the analysis of the χ^2 distribution), given the input assumptions. Some examples of the final fits to the entire SEDs are shown in Figure 2. Note that our simplistic models (which only

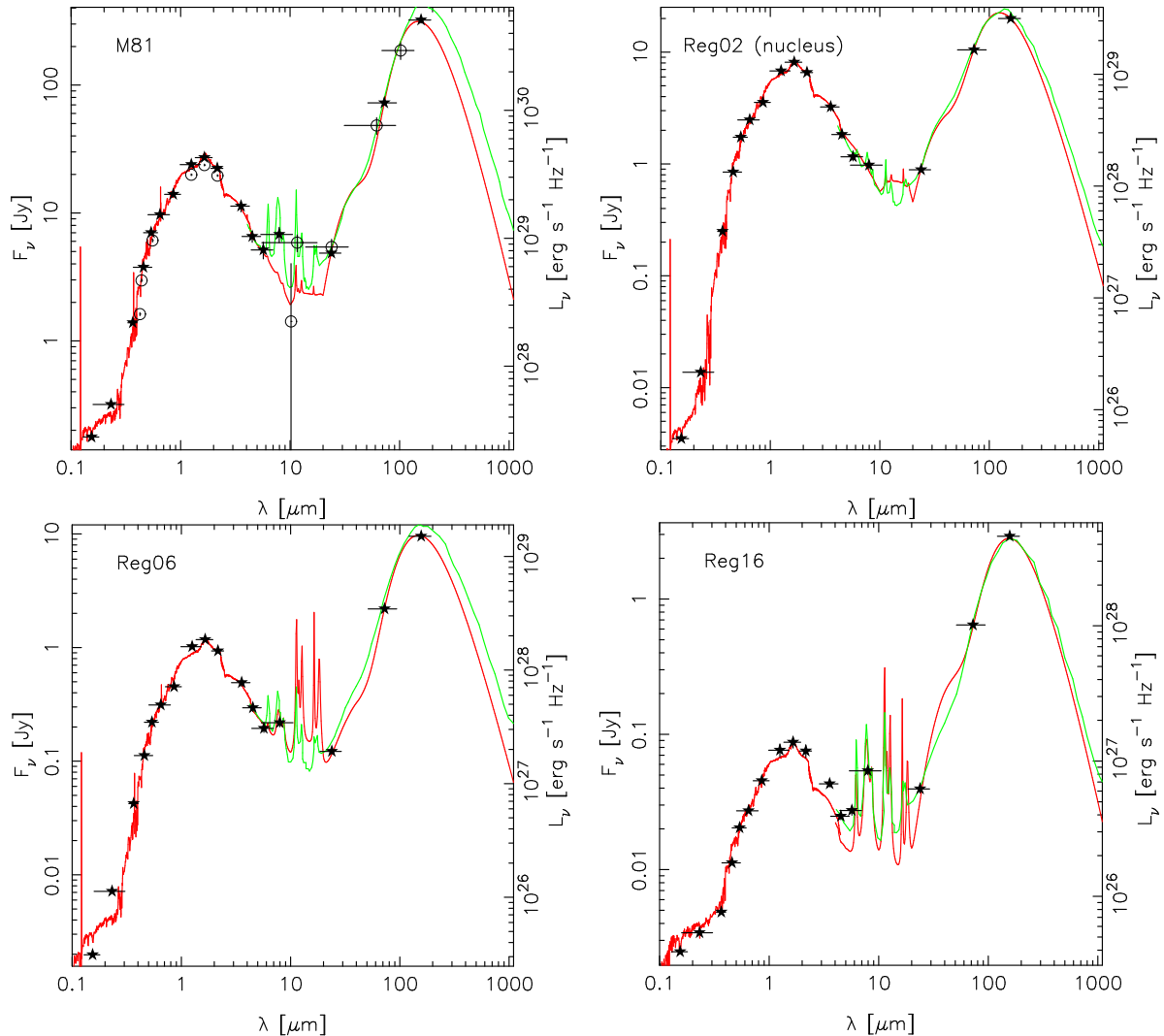


FIG. 2.— Spectral energy distributions for the entire M81 galaxy (upper-left panel), the nucleus (upper-right), and two regions in the arms (lower panels) selected at 160RES, corresponding to the photometry estimated with the global sky subtraction. The open circles in the SED of the entire galaxy refer to several photometric points extracted from NED (for apertures nearly as large as ours): three UV/optical fluxes from Code & Welch (1982) and de Vaucouleurs et al. (1992), the three NIR fluxes from 2MASS (Jarrett et al. 2000), the flux in the N -band from Kleinmann & Low (1970), and the four IRAS fluxes measured by Rice et al. (1988) and Devereux et al. (1995). Horizontal error bars for each photometry point show the width of the used filter. The data have been fitted (red line) to a model of the emission of the stars (a single burst with a exponential SFR), the gas (including the most common emission lines, shown in the plot with a width equal to the resolution of the stellar model at each wavelength), and the dust (including two dust components of two different temperatures, and aromatic molecules). Our models of the dust emission are compared with the ones carried out following the method in Draine et al. (2006, green line).

assume two dust temperatures) usually produce an artificial inflexion point at around $50\text{--}60\ \mu\text{m}$ (where the cold and warm dust components join). This artifact is also present in other models (for example, in the ones plotted in Figure 2 using the technique described in Draine et al. 2006), but it is not seen in any IR spectrum. However, it does not affect our estimates of the integrated IR luminosities, given that the energy output is dominated by emission at longer wavelengths.

The small number of independent observations in the MIR and FIR justifies the simplistic approach in our models with just three emitting components that need 5 free parameters to fit. We will use these models to estimate the integrated IR luminosities of regions in M81 and to study the characteristics of the dust in those re-

gions. We tested our results with other more complicated models (that use more free parameters and/or assumptions) to check that our approach did not introduce any systematic effects in those areas. We used comparison models developed by Dale & Helou (2002, see the next Section for more details) and Draine et al. (2006) to characterize all the SINGS galaxies. The latter models are based on the study of the Milky Way extinction carried out in Weingartner & Draine (2001). Briefly, these authors assume a certain stellar radiation field (based on the NIR data in our case) that heats the dust grains. The distribution of sizes of the dust grains is that observed for the Milky Way. The grain temperatures are calculated using a complete treatment of temperature fluctuations following single-photon heating and by studying

the thermal equilibrium of the dust. Figure 2 shows the comparisons of our fits and the ones carried out with the models by Draine et al. (2006). The fits are very similar, showing large differences only for wavelengths longer than $160 \mu\text{m}$, where the models by Draine et al. (2006) sometimes overpredict the observed flux. Despite this, our estimations of the TIR luminosities are very similar to those obtained from the comparison models (the average difference is less than 4%, with a scatter of 6%). However, the dust masses we obtain with our models are systematically smaller (on average, 0.2 ± 0.2 dex). This difference is linked to the sizes and composition of the grains assumed by each set of models. While we assume a fixed dust grain size and two dust temperatures, Draine et al. (2006) assume a dust size distribution based on Milky Way abundances, producing a range of temperatures. This size distribution includes larger amounts of cold dust than our two component fits. The difference in dust masses is comparable to the quoted uncertainties (see Figure 6) and does not affect our results.

3.3. Degeneracies of the models

Our stellar population synthesis models are subject to the typical degeneracies in this kind of study, for example age-metallicity (Worthey 1994) or extinction-age (see, e.g., Gil de Paz & Madore 2002, Pérez-González et al. 2003b, and Kauffmann et al. 2003).

The well-known age-metallicity degeneracy was artificially removed in our models by fixing the metallicity to the solar value based on estimates by several authors (Zaritsky et al. 1994; Stauffer & Bothun 1984; Kong et al. 2000).

The main source of degeneracy in our stellar emission models then comes from the lack of knowledge about the star formation history of the galaxy. Indeed, similar SEDs can be obtained with a young instantaneous ($\tau \sim 0$) burst or with older and less intense continuous star formation ($\tau \gg 1$). Therefore, our simplistic assumption of an exponentially decaying burst of star formation can be very far from the reality, where several small bursts may have occurred at different epochs. The final photometry would be, in general, blind to that formation history. However, given that M81 is an early-type spiral, it would be expected to have an old and massive burst forming the bulge, where most of the stars of the galaxy lie. This old stellar population would dominate the emission in the NIR. More recent star formation (switching on and off during the life of the galaxy) would be concentrated in the disk, with the most recent events contributing significantly to (or even dominating) the UV emission. Extinction can make the two scenarios previously described nearly indistinguishable.

However, the extinction and the lack of knowledge about the star formation history have only a minor effect on our results. In this paper, the models have been used to estimate the contribution of stellar light to the fluxes in the IRAC and MIPS bands. At these wavelengths, the extinction is negligible. Variations in the age or the star formation history do not strongly affect the shape of the SED in the NIR, particularly when the emission at these wavelengths is dominated by old stars (at least, for an early type spiral such as M81).

In the case of the dust emission models, there are two main degeneracies. The first comes from the lack of

knowledge about the aromatic spectrum in M81, and about the possibility of changes of that spectrum from region to region. Given this degeneracy, we will avoid any discussion about aromatic molecules in this paper. The second degeneracy is linked to the limited data in the FIR, which is unable to locate the emission peak accurately. Indeed, the SEDs seem to continue rising beyond our reddest point at $160 \mu\text{m}$ (or the maximum is reached at approximately that wavelength). Based on our models and the ones developed by Draine et al. (2006), we estimate that the lack of data at $\lambda > 160 \mu\text{m}$ leads to an uncertainty of less than a factor of 2 in the derived integrated IR luminosities and dust masses (which would be underestimated by our models if a significant amount of cold dust -with $T \lesssim 15$ K- is also present in M81). This uncertainty is smaller than the quoted errors. The absence of any data in the MIR between 24 and $70 \mu\text{m}$ should not affect the results significantly, since the energy in this wavelength regime is a small fraction of the total in the IR.

4. PROPERTIES OF THE DUST IN M81

In this Section, we will describe our main results on the properties of the dust in M81. All the results in this Section were obtained from the 160RES dataset because the dust emission is better characterized in this case (FIR data is available), and they span a larger range of radial distances, mapping most of the galaxy. We analyze the stellar and dust emission in the MIR from a statistical point of view, and estimate the integrated IR luminosity, which will be used in the comparison of SFR estimators in Section 5. We will specifically discuss the results obtained with the LOCALBKG photometry, where the calculated integrated luminosities refer to the dust heated only by the young stars, since the more diffuse emission (of more uncertain origin) is removed. We also include a discussion about the GLOBALBKG photometry, which might be useful for the study of the global stellar content in sub-galactic regions. In the last part of this Section, we will concentrate on the radial dependence of the dust properties in M81. Given that we are interested in the global characteristics of the dust, the results in the last subsection refer to the photometry measured with the regions selected at 160RES where the background was estimated globally (to include all the emission).

4.1. Stellar emission in the MIR

Our stellar population models show that the emission of the regions selected at 160RES is completely dominated by stars at $3.6 \mu\text{m}$ and $4.5 \mu\text{m}$, with very little contamination from the dust: the median and standard deviation of the fraction of the total emission coming from the dust for all the 160RES regions is $0 \pm 15\%$ at $3.6 \mu\text{m}$ and $0 \pm 10\%$ at $4.5 \mu\text{m}$. Stellar emission is also dominant at $5.8 \mu\text{m}$ ($40 \pm 20\%$ of the flux comes from the dust). At redder wavelengths, most of the emission comes from the dust: $80 \pm 20\%$ of the emission at $8 \mu\text{m}$, $93 \pm 7\%$ at $24 \mu\text{m}$, and $100 \pm 1\%$ at 70 and $160 \mu\text{m}$. These fractions are not affected by the intrinsic degeneracies of the modeling procedure, given that the models in this part of the spectrum are not very sensitive to changes in age or metallicity (the SEDs are dominated by the Rayleigh-Jeans spectrum of cold old stars), and the NIR and MIR are not strongly affected by extinction.

The fractions of the dust emission in the IRAC bands were checked using the recipe found in Pahre et al. (2004). The emission at 3.6 and 4.5 μm is assumed to be completely dominated by stars and we can estimate the contribution of the stellar emission to the 5.8 and 8.0 μm channels using the typical colors of an M0 III star [$m(3.6) - m(4.5) = -0.15$ mag, $m(4.5) - m(5.8) = +0.11$ mag, $m(5.8) - m(8.0) = +0.04$ mag in the Vega system, corresponding to $F_\nu(3.6)/F_\nu(4.5) = 1.78$, $F_\nu(4.5)/F_\nu(5.8) = 1.39$, and $F_\nu(5.8)/F_\nu(8.0) = 1.78$], which should dominate the stellar emission at these wavelengths. Using this recipe, we obtain an average dust contribution to the 5.8 and 8.0 μm emissions of $45 \pm 26\%$ and $77 \pm 22\%$, respectively.

Note that the regions used at 160RES enclose both star-forming complexes and/or zones of the arms where the emission is most probably dominated by older stars. The size of the photometry apertures has an effect on the stellar emission fractions previously quoted: for actual HII regions (i.e., for smaller apertures such as the 24RES ones) where the emission from young stars and warm dust is relatively more important, the fractions change by significant factors. According to our stellar population models, the 3.6 μm and 4.5 μm emissions have a non-negligible dust component: $10 \pm 10\%$ and $10 \pm 10\%$ of the total 3.6 and 4.5 μm flux comes from the dust, respectively. Note that heavily extinguished young stars that would be invisible in the optical could contribute to the observed flux in the NIR at 24RES. According to our models, the dust emission dominates the total flux at redder wavelengths: $70 \pm 20\%$ at 5.8 μm , $90 \pm 10\%$ at 8.0 μm , and $100 \pm 10\%$ of the total emission at 24 μm .

4.2. Integrated IR emission

In this Section, we use the regions selected in the 160RES image set to investigate possible relationships between monochromatic fluxes and colors in the MIR and FIR and the total emission of the dust integrated from 8 to 1000 μm [TIR luminosity, $L(8 - 1000)$ hereafter]. The following discussion will be mainly based on the photometry obtained for a GLOBALBKG. We will analyze the effect on these results of the diffuse IR emission by also using the photometry obtained with a LOCALBKG. This should give relationships which are better suited for SFR studies. The contribution of the stellar light has been subtracted from the MIR-FIR photometry prior to determining $L(8 - 1000)$.

4.2.1. The estimation of $L(8 - 1000)$

TIR luminosities were calculated for the 160RES regions by integrating the fitted dust models. We also calculated the integrated luminosity from 3 to 1100 μm [$L(3 - 1100)$] to compare our data with the semi-empirical models developed by Dale & Helou (2002). These authors obtained an equation (Equation 4 in that paper) to estimate the $L(3 - 1100)$ from the three MIPS fluxes. This relationship is based on models of the global emission of normal star-forming galaxies with $L(3 - 1100) \gtrsim 10^8 L_\odot$. Thus, the application to faint individual HII regions within a galaxy may not be justified. In fact, the SEDs for sub-galactic regions in M81 are colder than the coldest model in the Dale & Helou (2002) template set, as also noted by Dale et al. (2005) for sub-galactic re-

gions in M51 and NGC7331, and by Helou et al. (2004) for NGC300.

For the GLOBALBKG photometry, our own estimations of $L(3 - 1100)$ are systematically fainter (7% on average, with a scatter of 6%) than the ones obtained using Equation 4 in Dale & Helou (2002). The scatter is mainly due to the two nuclear regions and the coldest regions in the inter-arm zone; without these regions, the scatter is 2%. For the entire galaxy, our models give a value of $L(3 - 1100)$ that is 1% lower than the one obtained with the equation in Dale & Helou (2002). These small systematic differences (comparable to the uncertainties in the measured MIPS fluxes) are consistent with the fact that the sub-galactic regions in M81 are colder than the coldest model in the Dale & Helou (2002) template set.

If we use the photometry calculated with the LOCALBKG, the values of $L(3 - 1100)$ estimated from our models are 5-15% lower than the ones for the GLOBALBKG. This is mainly caused by a decrease in the 160 μm flux due to the substantial diffuse emission at that wavelength. The diffuse component accounts on average for 36% of the total 8 μm emission of the 160RES regions, 23% at 24 μm , 26% at 70 μm , and 34% at 160 μm . The average difference between our luminosities (for the LOCALBKG, i.e., after subtracting the diffuse emission) and those estimated with the Equation in Dale & Helou (2002) is $10 \pm 3\%$. In this case, there is a clear linear correlation where the difference is higher for fainter regions: up to 15% for the faintest source at $L(3 - 1100) \sim 10^{6.8} L_\odot$ and 5% for the brightest at $L(3 - 1100) \sim 10^8 L_\odot$.

These comparisons suggest that the equations derived for entire galaxies with high IR luminosities should be corrected by small amounts when applying them for sub-galactic regions with moderate SFRs (and for entire galaxies with low IR luminosities). The reason is that the emission of the cold dust is relatively brighter for pieces of galaxies or galaxies with moderate SFRs and dust contents, and the diffuse emission plays an important role. This diffuse emission is extremely relevant for the wavelengths around 160 μm , which contribute the most to the TIR luminosity, as we show in the following discussion.

4.2.2. Correlating the three MIPS fluxes to $L(8 - 1000)$

Relying on our models of dust emission for the different 160RES regions in M81, we obtained simple relationships (using a singular value decomposition method) to obtain $L(8 - 1000)$ and $L(3 - 1100)$ from the fluxes at the three MIPS wavelengths (after subtracting the stellar component) for sub-galactic regions in the range $10^7 \lesssim L(8 - 1000) \lesssim 10^8 L_\odot$. In all the following Equations, $L(\text{filter})$ refers to $\nu_{\text{eff}} L_\nu$ in units of erg s^{-1} or solar units, where ν_{eff} is the effective frequency of the filter. The relations for the GLOBALBKG case, in solar units, are¹³:

$$L(8 - 1000) = (+1.439 \pm 0.415) \times L(24) + (+0.814 \pm 0.099) \times L(70) + (+1.1229 \pm 0.039) \times L(160) \quad (2)$$

¹³ All the correlations in this Section have been obtained by fitting the data for sub-galactic regions (i.e., not using the data point for the entire galaxy) and accounting for the uncertainties.

$$L(3 - 1100) = (+1.832 \pm 0.420) \times L(24) + (+0.779 \pm 0.094) \times L(70) + (+1.176 \pm 0.031) \times L(160) \quad (3)$$

For both fits, the data show a scatter of 1% around the given relationships.

The same equations for luminosities estimated after subtracting the diffuse emission (LOCALBKG case) are:

$$L(8 - 1000) = (+0.202 \pm 0.510) \times L(24) + (+0.802 \pm 0.160) \times L(70) + (+1.303 \pm 0.061) \times L(160) \quad (4)$$

$$L(3 - 1100) = (+0.294 \pm 0.551) \times L(24) + (+0.766 \pm 0.190) \times L(70) + (+1.392 \pm 0.063) \times L(160) \quad (5)$$

The scatter of the data points around these relations is approximately 4% in both cases.

4.2.3. Correlating monochromatic MIR fluxes to $L(8 - 1000)$

Given the poorer resolution of the MIPS 70 and 160 μm channels relative to the 24 μm channel, it would be very convenient to use the 24 μm emission alone to obtain reliable IR luminosities. This would allow us to study the star-forming complexes in M81 (or any other resolved galaxy) at high enough angular resolution to resolve individual HII regions and compare the IR results with other SFR estimators, such as $\text{H}\alpha$ or the UV.

The degree of reliability of using only one monochromatic flux to estimate the 8-1000 μm luminosity is shown in Figure 3, including the diffuse emission at all wavelengths (left panel) and removing it (right panel). Here we plot the TIR luminosity of each individual region estimated with the three MIPS fluxes (after removing the stellar component) as a function of the monochromatic luminosity in those MIPS bands. The best fits to the GLOBALBKG data are the following (with all luminosities in solar units):

$$\log [L(8 - 1000)] = (+0.63 \pm 0.11) + (+1.020 \pm 0.015) \times \log [L(8.0)] \quad (6)$$

$$\log [L(8 - 1000)] = (+1.25 \pm 0.06) + (+0.997 \pm 0.010) \times \log [L(24)] \quad (7)$$

$$\log [L(8 - 1000)] = (+1.71 \pm 0.46) + (+0.839 \pm 0.065) \times \log [L(70)] \quad (8)$$

$$\log [L(8 - 1000)] = (-0.27 \pm 0.36) + (+1.064 \pm 0.048) \times \log [L(160)] \quad (9)$$

The diffuse emission has a very significant effect on the previous correlations, especially for the 8 and 160 μm data. The relationships between the monochromatic fluxes and the TIR luminosity for the photometry where the diffuse emission has been removed (LOCALBKG case) are:

$$\log [L(8 - 1000)] = (+0.95 \pm 0.13) +$$

$$+ (+0.980 \pm 0.019) \times \log [L(8.0)] \quad (10)$$

$$\log [L(8 - 1000)] = (+1.88 \pm 0.27) + (+0.897 \pm 0.041) \times \log [L(24)] \quad (11)$$

$$\log [L(8 - 1000)] = (+1.78 \pm 0.27) + (+0.824 \pm 0.038) \times \log [L(70)] \quad (12)$$

$$\log [L(8 - 1000)] = (-0.14 \pm 0.30) + (+1.050 \pm 0.041) \times \log [L(160)] \quad (13)$$

Figure 3 clearly shows that the best estimator of the TIR luminosity (the one presenting the lowest scatter) is the 160 μm emission, which accounts for more than 50% of the TIR luminosity (see also Equations 2 and 4). The scatter around a linear relationship for the monochromatic 160 μm data is 5% of the TIR luminosity (6% if we remove the diffuse emission). The 24 μm data alone is a much poorer estimator of the TIR luminosity, presenting a scatter around the given relationship of 12% (13%). The goodness of the 70 μm and the 8 μm data as estimators of the TIR luminosity lies in between: 9% (11%) and 8% (7%) scatter around the given relationships, respectively. It is important to notice that, although 8.0 μm seems to be a better TIR luminosity estimator than 24 μm based on the scatters of the fits, the IRAC band is more affected by the stellar emission contamination (more than a factor of 2 difference). Moreover, the 8.0 μm image shows a brighter diffuse emission component than the 24 μm image, 36% of the total emission for the former and 23% for the latter (cf. Section 4.2.1). According to Fazio et al. (2004), the scattered light in the 8 μm array can only account for $\sim 2\%$ of that fraction. This clearly shows that the 8 μm emission depends not only on the local star formation rate but also in some other mechanisms related to the formation and destruction of aromatic molecules (see Calzetti et al. 2005, and references therein). Indeed, in the LOCALBKG case (where the starlight contamination and the diffuse emission of uncertain origin should be removed), the correlation between the 8 μm and the TIR luminosities improves.

Figure 3 also shows one interesting point about the contribution of the various wavelengths to the integrated luminosity. As we move to higher TIR luminosities, the contribution of the 160 μm luminosity to the integral becomes less important (as the positive slope shows), while the contribution of the hotter dust emitting at shorter wavelengths rises (as shown by the negative slopes of the linear fits for 24 and 70 μm). Figure 3 shows that the dust contributing the most to $L(8 - 1000)$ has a temperature of around $T \sim 19$ K (its emission peaks at $\lambda \sim 160$ μm) for $L(8 - 1000) \lesssim 10^8 L_\odot$. The fraction of $L(8 - 1000)$ emitted by the dust at $T \gtrsim 40$ K (with emission peaking at $\lambda < 70$ μm) increases as $L(8 - 1000)$ gets brighter (i.e., as the current SFR increases). The hotter dust contributes as much as the colder dust component at $L(8 - 1000) \gtrsim 10^{8.5} L_\odot$ (i.e., for $SFR \gtrsim 0.05 \mathcal{M}_\odot \text{yr}^{-1}$). The fraction of $L(8 - 1000)$ emitted by dust at $T \gtrsim 125$ K (with emission peaking at 24 μm) is always lower than 10% for $L(8 - 1000) \lesssim 10^{9.0} L_\odot$. Another interesting

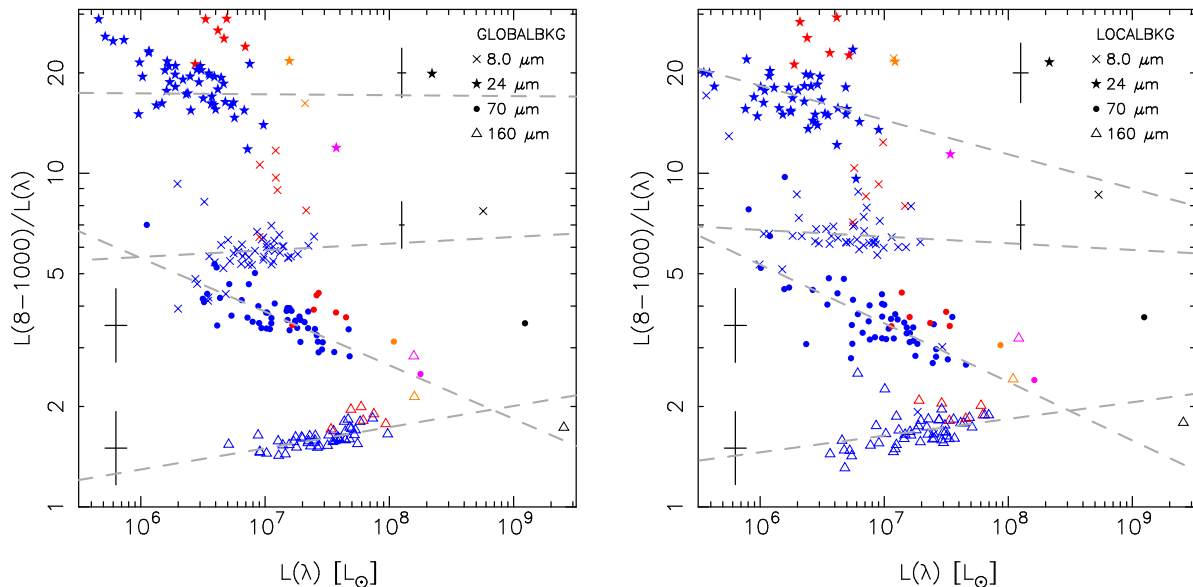


FIG. 3.— Relationship between the MIR and FIR monochromatic emissions and the 8-1000 μm luminosities for star-forming complexes in M81 (selected in 160RES resolution images). On the left panel, the data refer to the photometry calculated with a global background (GLOBALBKG case in the text). On the right, a local background (LOCALBKG case) was used to remove the diffuse component of the emission in the IR. For both panels, the integrated luminosities have been calculated by fitting models of dust emission to the SEDs for wavelengths redder than 5 μm . The best linear fits to the data at each wavelength are also shown. The different colors refer to the distinct types of regions defined in the left panel of Figure 1. In both panels, average errors for the different luminosities (horizontal bars) and luminosity ratios (vertical bars) are plotted to one side of the corresponding data points.

point in Figure 3 is that the regions dominated by diffuse emission (red symbols) seem to deviate significantly from the star-forming complexes (blue symbols), showing a larger contribution to $L(8 - 1000)$ from the colder dust.

Finally, it is also worth noticing that the entire galaxy and the nuclear and circumnuclear zones deviate significantly from the relationship found for the star-forming regions in the arms of M81. These regions present systematically hotter dust temperatures than the ones obtained for the zones in the arms (see Section 4.3), which should be linked to other sources of heating, such as the central AGN, the bulge old stars, or dynamical friction (Gordon et al. 2006).

4.2.4. Correlating MIR colors to $L(8 - 1000)$

In Figure 4, we explore the possibility of using a color to improve the relationship between the 24 μm and the TIR luminosities. In principle, we could expect a color involving MIR fluxes to be correlated with the behavior of the SED in the FIR, i.e., the amount and emissivity of the cold dust (dominating the FIR luminosity) might be linked with the properties of the warm dust if both dust components share the same heating source. If that were the case, we would be able to reduce the scatter in the estimation of $L(8 - 1000)$ from single MIR fluxes. Figure 4 shows that there is a correlation between the 8.0 μm -to-24 μm color and the TIR luminosity, although the scatter is considerable. The best fit to the data (GLOBALBKG case) gives:

$$\log[L(8 - 1000)/L(24)] = (+0.94 \pm 0.05) + (-0.644 \pm 0.102) \times \log[L(24)/L(8.0)] \quad (14)$$

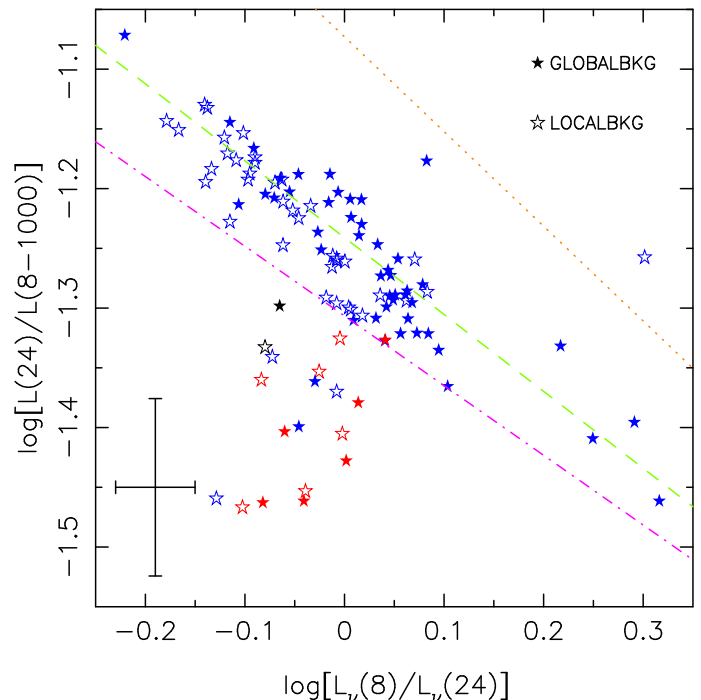


FIG. 4.— The 24-to-TIR luminosity ratio as a function of the 8.0-to-24 μm color for different regions selected in the 160RES image set. Filled stars show the results for the photometry calculated with a global background, and open stars for the local background. From top to bottom, the linear relationships show the correlations found by Calzetti et al. (2005) for 21 regions in M51 (dotted line), our own correlation (dashed line), averaged from Equations 14 and 15, and the prediction from the models of Dale & Helou (2002, dash-dotted line). The different colors refer to the distinct types of regions defined in the left panel of Figure 1.

For the data where the diffuse component has been removed (LOCALBKG case), the correlation is very similar:

$$\log [L(8 - 1000)/L(24)] = (+0.93 \pm 0.06) + (-0.695 \pm 0.155) \times \log [L(24)/L(8.0)] \quad (15)$$

Using this relationship, we are able to reduce the scatter in the determination of $L(8 - 1000)$ to less than 6% (11% for the photometry with no diffuse emission), i.e., the estimates are two times better than the ones obtained using 24 μm alone. However, the correlation has a significant number of outliers, most of them corresponding to regions where the star formation is not very high and the diffuse emission is very important (inter-arm regions and zones between the arms and the nucleus). Our correlation lies very near the predictions from the models of Dale & Helou (2002), and it is significantly different from the relationship found by Calzetti et al. (2005) for 21 regions in M51, although the slope is very similar. These differences must arise from the fact that the 8-to-24 μm color depends on the strength of the aromatic emission (contributing mainly at 8 μm), which presents significant variations from galaxy to galaxy depending on parameters such as the abundance of aromatic molecules, composition (linked to the metallicity, see Engelbracht et al. 2005), or temperature of the galaxy (see Dale et al. 2005). Therefore, one should be cautious in using Equations 14 and 15 for any galaxy before it is checked for a larger sample.

All the correlations found in this Section are summarized in Table 3.

4.3. Spatially resolved properties of the dust in M81

Figure 5 shows the MIPS colors as a function of radius (de-projected radial distances) for the regions selected from the 160RES dataset¹⁴. In our models, the radial dependence of the MIPS colors manifests as a radial gradient in the dust temperature. The model dust temperatures as a function of radius are plotted in the insets of Figure 5. This figure shows that the IR emission in M81 is dominated by a cold dust component having temperatures around 18 K (the average and standard deviation are $\langle T_c \rangle = 18 \pm 2$ K). The warmer dust component has an average temperature of $\langle T_w \rangle = 53 \pm 7$ K. In comparison with these temperatures, Devereux et al. (1995) obtain an average dust temperature of $T \sim 30$ K (approximately the average of our two components) for the entire galaxy and just using the IRAS 60 and 100 μm fluxes and models with a single dust component. Devereux et al. (1995) also provide expected values for the temperature profiles of the dust. The temperatures in these profiles range from $T \sim 15$ K to $T \sim 50$ K (depending on the composition of the dust), values that are very similar to the ones obtained for our fits. Our dust temperatures are also comparable to those estimated from other work based on FIR and sub-mm data, which find cold dust temperatures of 15–25 K and warm dust temperatures of 40–60 K (Dunne et al. 2000; Dunne & Eales 2001; Popescu et al. 2002; Bendo et al. 2003; Regan et al. 2004; Engelbracht et al. 2004)

The cold dust component shows a clear trend of decreasing temperature with increasing radius, although the scatter and fitting errors are large. The temperature profile is consistent with the observed radial gradient of the $L(160)/L(70)$ color, which increases from $L(160)/L(70) \sim 2$ to $L(160)/L(70) = 3 - 4$ within the disk. For the warm dust component, the temperature radial gradient is very small, resulting from a change in the $L(160)/L(24)$ color of a factor of 2 from the center to the outskirts of M81. The central regions of M81 show slightly hotter dust temperatures in the cold component: $T_c = 22.8 \pm 1.0$ K and $T_c = 21.6 \pm 0.5$ for the nuclear and circumnuclear regions, respectively. As we mentioned earlier, this could be due to the presence of another efficient source of dust heating, apart from the young stars: an AGN for the nucleus and/or older stars (whose density is higher in the bulge of the galaxy and may present radial changes in the stellar SEDs) for both zones (see Genzel & Cesarsky 2000, and references therein). These effects could also be responsible for the radial gradient in the cold dust temperatures.

In combination with the radial gradient of the dust temperature, our models also reveal a decrease in the dust mass surface density as we move to higher radial distances (beyond $\sim 300''$). This is shown in Figure 6, where we use de-projected radial distances and surface densities. This figure also shows the profile through the major axis of M81 for the mass surface density of the atomic and molecular gas (estimated by Devereux et al. 1995 using the data in Gottesman & Weliachew 1975 and Rots & Shane 1975 for the atomic gas, and using the ^{12}CO intensities measured by Brouillet et al. 1991 and Sage & Westpfahl 1991). For the entire galaxy, the dust-to-gas ratio is 0.005 (accounting for both atomic and molecular gas). We detect a factor of 10 increase in the dust mass surface density from the center of the galaxy to the inner part of the arms (at a radial distance of approximately 200''). The atomic gas surface density also increases by a similar amount in the same region. Within the arms (from $\sim 200''$ to $\sim 400''$), the dust mass density is about $10^{5.9} \mathcal{M}_\odot \text{kpc}^{-2}$ (with a scatter of about 0.2dex). The regions with the highest dust mass surface densities are found at radial distances of 300–350'', just where the profiles for the molecular and atomic gas surface densities peak. The dust mass surface density decreases (by roughly a factor of 10) from $\sim 300''$ to the outer regions. This gradient in the dust density should produce a radial decrease in the extinction of the stellar light, which is confirmed in Section 5 (see Figure 11).

One caveat to our results on the radial gradient of the dust mass density arises from the lack of data at wavelengths longer than 160 μm ¹⁵, where the peak of the SED must be located. Our data are not sufficient to accurately delimit the position of that maximum, which results in relatively large uncertainties on the amount of dust and emission arising from dust colder than approximately 20 K. This means that our estimations of the dust mass should be considered as lower limits. More data in the sub-millimeter range (at least, at wavelengths redder than $\sim 200 \mu\text{m}$, the range that will be covered by

¹⁴ The results in this Subsection refer to the GLOBALBKG case, since we are studying the properties of all the dust emission in M81, including the diffuse component.

¹⁵ The only data available for M81 in the sub-mm is a JCMT/SCUBA observation of the central 2' of the galaxy which do not cover any of the star-forming complexes in the arms.

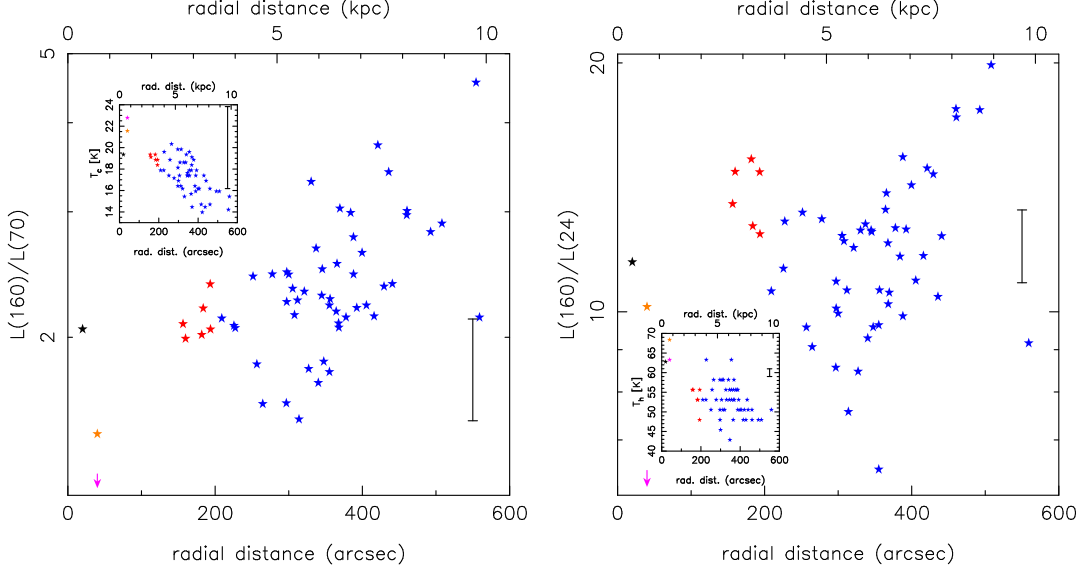


FIG. 5.— Radial plots (using de-projected radial distances) of the MIPS colors for the regions selected at 160RES. The different colors refer to the distinct types of regions defined in the left panel of Figure 1. The average surface density of the entire galaxy has been plotted at $r = 20''$, and the surface density for the nuclear and the circumnuclear regions has been plotted at $r = 40''$ (slightly shifted from $r = 0$ for clarity). The insets in each panel show the dust temperatures for the cold (left panel) and warm (right panel) components in our models. Average errors for the colors and temperatures are shown in each panel.

TABLE 3
SUMMARY OF CORRELATIONS BETWEEN MID-INFRARED MONOCHROMATIC LUMINOSITIES AND COLORS AND THE INTEGRATED IR LUMINOSITIES.

Estimator	BKG	A	$B(8.0)$	$B(24)$	$B(70)$	$B(160)$	σ
$L(8 - 1000)$	GLOBAL ^a	$+1.439 \pm 0.415$	$+0.814 \pm 0.099$	$+1.1229 \pm 0.039$	1%
$\log [L(8 - 1000)]$	GLOBAL	$+0.63 \pm 0.11$	$+1.020 \pm 0.015$	8%
	GLOBAL	$+1.25 \pm 0.06$...	$+0.997 \pm 0.010$	12%
	GLOBAL	$+1.71 \pm 0.46$	$+0.839 \pm 0.065$...	9%
	GLOBAL	-0.27 ± 0.36	$+1.064 \pm 0.048$	5%
	GLOBAL	$+0.94 \pm 0.05$	$+0.644 \pm 0.102$	$+0.356 \pm 0.102$	6%
$L(8 - 1000)$	LOCAL ^a	$+0.202 \pm 0.510$	$+0.802 \pm 0.160$	$+1.303 \pm 0.061$	4%
$\log [L(8 - 1000)]$	LOCAL	$+0.95 \pm 0.13$	$+0.980 \pm 0.019$	7%
	LOCAL	$+1.88 \pm 0.27$...	$+0.897 \pm 0.041$	13%
	LOCAL	$+1.78 \pm 0.27$	$+0.824 \pm 0.038$...	11%
	LOCAL	-0.14 ± 0.30	$+1.050 \pm 0.041$	6%
	LOCAL	$+0.93 \pm 0.06$	$+0.695 \pm 0.155$	$+0.305 \pm 0.155$	11%
$L(3 - 1100)$	GLOBAL ^a	$+1.832 \pm 0.420$	$+0.779 \pm 0.094$	$+1.176 \pm 0.031$	1%
$L(3 - 1100)$	LOCAL ^a	$+0.294 \pm 0.551$	$+0.766 \pm 0.190$	$+1.392 \pm 0.063$	4%

NOTE. — The Table shows the coefficients of the correlations (in logarithmic scale except for the correlations involving the 3 MIPS wavelengths) between the MIR and FIR monochromatic luminosities and the total IR luminosity integrated between 8 and 1000 μm [$L(8 - 1000)$] and 3 and 1100 μm [$L(3 - 1100)$]. The equation for each correlation is: $\log [L(8 - 1000)] = A + \sum_i B(\lambda_i) \times \log L(\lambda_i)$ [except for the correlation between the 3 MIPS luminosities and the integrated IR emission, where the correlation is $L(8 - 1000) = \sum_i B(\lambda_i) \times L(\lambda_i)$]. The sum extends over the wavelengths of the last IRAC channel and the 3 MIPS bands (8.0, 24, 70, and 160 μm). In the last column, σ represents the scatter of the data around the given relation. All luminosities are given in erg s^{-1} .

^aThis correlation is given in linear scale, not logarithmic.

Herschel) are necessary to account for the coldest dust component and robustly estimate the total amount of dust.

5. COMPARISON OF STAR FORMATION RATE ESTIMATORS

In this Section, we compare different SFR tracers for 59 individual HII regions in M81 with available extinction measurements. All of these HII regions are resolved in our 24RES image set (see the right panel of Figure 1).

The sample of 59 sources includes the 18 HII regions in the disk and outskirts of M81 (at radial distances between 3 and 15 kpc) for which Garnett & Shields (1987) obtained optical spectra. These authors measured Balmer decrements that, appropriately corrected for stellar absorption and temperature effects, provide a good estimate of the extinction of the gas emission. The remaining 42 sources in our sample are giant HII regions (at radial distances between 3 and 10 kpc) for which

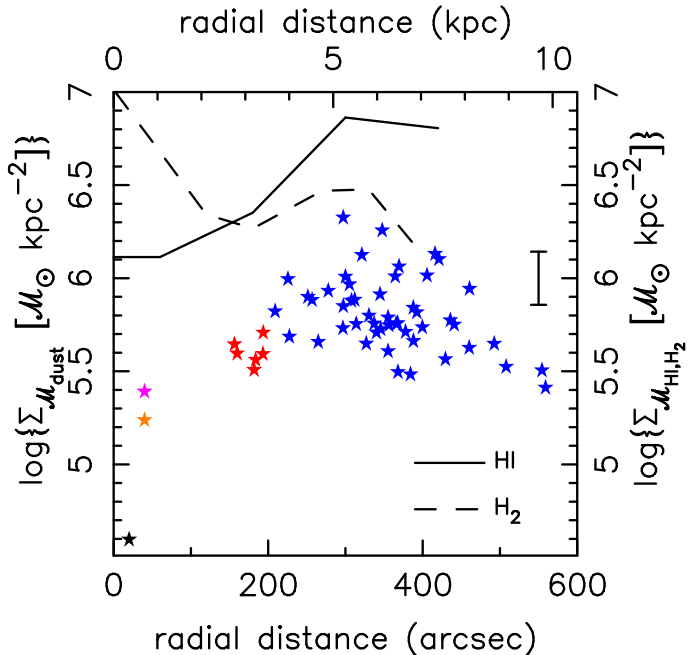


FIG. 6.— Radial profile (using de-projected radial distances) of the dust mass surface density (also corrected for inclination). The different colors refer to the distinct types of regions defined in the left panel of Figure 1. The average surface density of the entire galaxy has been plotted at $r = 20''$, and the surface density for the nuclear and the circumnuclear regions has been plotted at $r = 40''$ (slightly shifted from $r = 0$ for clarity). The profiles through the major axis for the mass surface density of the atomic gas (continuous line) and molecular gas (dashed line, Devereux et al. 1995) are also plotted, with the scale shown on the right vertical axis.

Kaufman et al. (1987) obtained $H\alpha$ and radio (at 6 and 20 cm) observations, estimating optical extinctions for most of them. These extinction estimations may be affected by radio synchrotron emission not directly linked to the recent star formation (Condon 1992).

In the following, we compare the luminosities of the HII regions in M81 for 5 SFR tracers: the UV emission, the $H\alpha$ nebular emission, and 3 luminosities in the IR wavelength range [$L(8 - 1000)$, $L(24)$, and $L(8)$, all referring to the photometry measured with a LOCAL-BKG]. In this comparison of SFR estimators, we also include the results obtained by Calzetti et al. (2005) for the central region of M51. In that work, $H\alpha$ and $P\alpha\alpha$ narrow-band fluxes, jointly with IRAC and MIPS emissions, are measured for HII regions with high extinctions ($1 < A(V) < 4$). The combination of the data for M81 and M51 allows us to probe a wide range of attenuations (from $A(V) \sim 0$ to $A(V) \sim 4$) and SFRs (from 3×10^{-4} to $0.1 M_{\odot} \text{ yr}^{-1}$, or 5×10^{-3} to $0.3 M_{\odot} \text{ yr}^{-1} \text{ kpc}^{-2}$).

The extinction corrected $H\alpha$ luminosities used in this Section have been estimated by adopting the following differential values between the $H\alpha$, $H\beta$, and $P\alpha\alpha$ attenuation factors, $k(\lambda)$ ¹⁶: $k(H\beta) - k(H\alpha) = 1.23$ and $k(H\alpha) - k(P\alpha\alpha) = 2.02$, with $k(H\alpha) = 2.41$. These factors correspond to a screen attenuation law with $A(V) \sim 0.5$ for M81 and $A(V) \sim 3.0$ for M51, homo-

geneous distribution of the dust, and dust properties typical of the Small Magellanic Cloud (Witt & Gordon 2000). These attenuation laws seem to best reproduce the observations for M81 (see, e.g., Hill et al. 1995) and M51 (see Calzetti et al. 2005). Other attenuation laws in Witt & Gordon (2000) with different star-dust geometries and distributions, or extinction laws such as the ones in Cardelli et al. (1989), provide similar factors (different by less than 1%). We have assumed the theoretical line ratios $H\alpha/H\beta = 2.86$ and $H\alpha/P\alpha\alpha = 8.46$, values expected for a low density gas ($n_e = 10^2 \text{ cm}^{-3}$) with $T_e = 10^4 \text{ K}$ in the recombination Case B including collisional effects (Osterbrock 1989).

5.1. The TIR luminosity as a SFR tracer

The left panel of Figure 7 shows the comparison between the TIR luminosity (calculated with Equation 15) and the extinction corrected $H\alpha$ emission for the HII regions in M81 and M51. The best linear fit to the data for both galaxies is¹⁷:

$$\log\{L(8 - 1000)\} = (+2.3 \pm 1.2) + (+0.992 \pm 0.031) \times \log\{L^{\text{corr}}(H\alpha)\} \quad (16)$$

The scatter of the data around this relationship is 30%. This equation is very different from the one obtained by Calzetti et al. (2005) for the M51 regions alone. In fact, Figure 7 (see the inset in the left panel) shows that the M81 and M51 data points seem to follow different trends. The slopes obtained for the M81 or the M51 data alone are very similar (~ 0.9), but there is an offset in the zero point (shown in the inset by the offset in the cloud of points for both galaxies). For the same value of $L^{\text{corr}}(H\alpha)$, the M51 regions are brighter than the M81 ones in the IR. This offset is consistent with the larger $A(V)$ values found for the M51 central region in comparison with the extinctions found for the HII regions in the arms of M81. For the regions with larger extinctions (the ones in M51), more energy is absorbed by the dust and reemitted in the IR.

Classically, total SFRs for galaxies (or pieces of galaxies) have been obtained in two different ways. One option is using an estimator affected by dust attenuation, such as an emission-line or the UV emission, and correcting the observed flux for the effects of extinction. Another possibility is directly using a SFR tracer that is not affected by dust attenuation, such as the IR or radio emission. Both ways of estimating total SFRs were compared in the left panel of Figure 7 (where we compare extinction-corrected $H\alpha$ luminosities with TIR luminosities). In principle, the IR emission is linked to the dust heated by the light coming from the newly-formed stars in the HII regions. The UV and $H\alpha$ emissions (without any extinction correction) are linked to the photons arising from those young stars that do not interact with the dust at all. This means that we can obtain an estimate of the SFR from the observed $H\alpha$ or the UV emission that cannot be detected by the IR because these photons do not interact with the dust, and on the other hand, we can account for the emission-line or UV photons which are extinguished by dust by using IR obser-

¹⁶ The attenuation at a given wavelength, $A(\lambda)$, is given by $A(\lambda) = k(\lambda) \times E(B - V)$

¹⁷ All the linear correlations in this Section will be given for luminosities in units of erg s^{-1} .

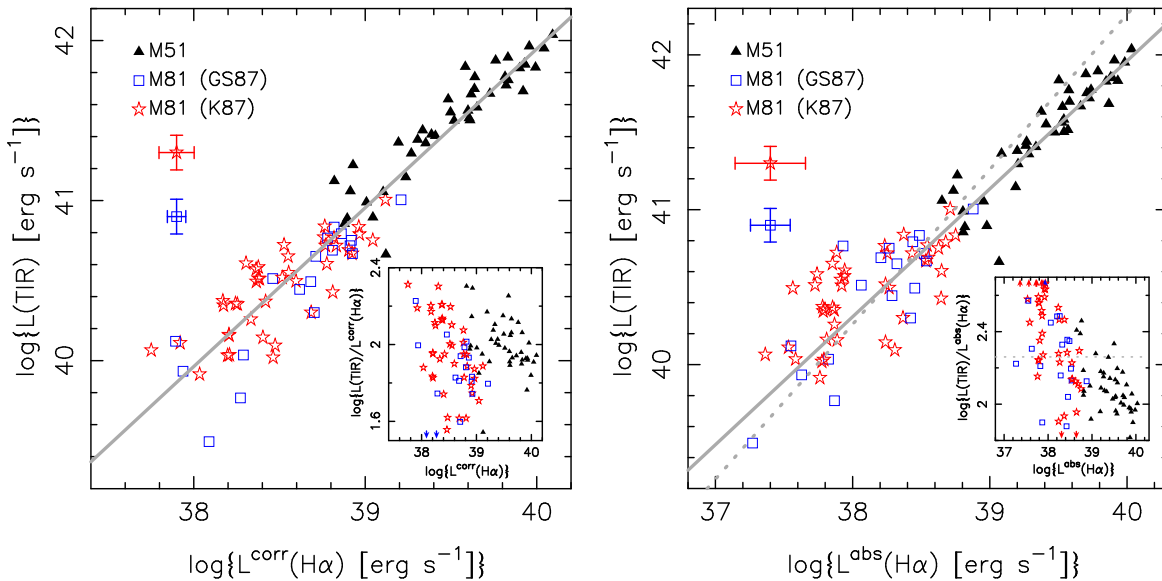


FIG. 7.— On the left, comparison between the extinction corrected $H\alpha$ and the TIR luminosities for selected HII regions in M81 (with different colors and symbols referring to the distinct types of regions defined in the right panel of Figure 1, extracted from Garnett & Shields 1987 -GS87- and Kaufman et al. 1987 -K87-) and in M51 (black triangles; data extracted from Calzetti et al. 2005). On the right, the TIR luminosity of the same sample of HII regions is compared with the $H\alpha$ luminosity absorbed by the dust. For both panels, we show the typical uncertainties linked to each catalog of HII regions in M81. The best linear fit is plotted with a continuous gray line. The insets show the same plots but using a luminosity ratio in the vertical axis to enhance the differences in the trends followed by the datasets for each galaxy. The dotted line in the right panel (and the inset) shows the luminosity relation for slope unity and a ratio between the $H\alpha$ and TIR luminosities given by the SFR calibrations found in Kennicutt (1998).

vations. Consequently, an alternative way to obtain a total SFR would be to add the 'unobscured SFR' derived in the UV/optical (without any extinction correction) and the 'obscured SFR' obtained from the IR luminosity (see Kennicutt et al. 2006). This total SFR should be the same as the SFR derived with the UV/optical estimators after correcting them for the effects of extinction and taking into account the spatial variations of the dust content in star-forming regions, which might result in the UV/optical and IR emissions arising from different regions (with different attenuations). It should also coincide with the SFR derived with the IR emission alone, if we can obtain a calibration for it that takes into account the amount of star formation not obscured by dust (or if this star formation is negligible in comparison with the star formation hidden by dust).

The alternative method of obtaining the total SFR adding the estimations of the unobscured SFR (obtained with the observed $H\alpha$ or/and UV luminosities) and the obscured SFR (obtained with the IR emission) requires the existence of a (simple) correlation (close to pure proportionality) between the extinguished correction for the UV/optical SFR tracers and the emission in the IR. The right panel of Figure 7 explores this correlation for the TIR luminosity, comparing it with the $H\alpha$ luminosity extinguished by dust ($L^{\text{abs}}(H\alpha)$, calculated by subtracting the observed luminosity from the extinction corrected luminosity) for the HII regions in M81 and M51. The best linear fit to the data is:

$$\log\{L(8-1000)\} = (+8.9 \pm 1.0) + (+0.826 \pm 0.025) \times \log\{L^{\text{abs}}(H\alpha)\} \quad (17)$$

The scatter of the data around this relationship is 30%. The scatter of the points for the M81 data is larger than

for the M51 data (45% and 20%, respectively). Most of this scatter (and the scatter observed in all the panels in Figures 7 through 9) is due to the larger uncertainties in the extinctions derived for the HII regions in M81 in comparison with the $P\alpha\alpha$ -to- $H\alpha$ derived extinctions for M51. The scatter might also be caused by spatial changes in the extinction properties within an individual HII region (i.e., the actual net extinction and the attenuation law). If the central parts of the HII regions had larger extinctions than the outskirts, our values of $L^{\text{corr}}(H\alpha)$ would be overestimated. To test this effect, we measured fluxes for the same HII regions but with smaller apertures. The correlation was slightly better in this case, with a scatter around the linear relationship of 25%.

The different trends shown by the M81 and M51 data in the inset of the left panel of Figure 7 disappear in this plot, although the scatter of points is slightly larger, mostly because of the M81 points (and especially the ones with extinctions estimated with radio data). In addition, the slope of the correlation differs significantly from unity (0.826 ± 0.025), the value that is expected if the two quantities are closely correlated. This behavior suggests that the heating of the colder dust, which dominates the TIR luminosity, is not directly caused (exclusively) by the Lyman photons. The right panel of Figure 7 also shows the luminosity relation with slope unity and a ratio between the $H\alpha$ and TIR luminosities given by the SFR calibrations found in Kennicutt (1998). Note that Kennicutt's calibration was built for entire starburst galaxies assuming continuous star formation for the last 10–100 Myr. Despite this, the relation fits the data points for the M81 HII regions very well, but it departs significantly from the brightest M51 points. This effect indicates differences in the attenua-

tion properties (for example, in the attenuation law) of the mildly extinguished M81 regions in comparison with the heavily attenuated M51 central zone.

5.2. The rest-frame 24 μm luminosity as a SFR tracer

For the nuclear region of M51, Calzetti et al. (2005) found that the 24 μm emission correlates tightly (even better than the TIR luminosity) with the extinction corrected $\text{Pa}\alpha$ luminosity, suggesting that the warm dust responsible for the 24 μm emission is heated by the ionizing photons. Indeed, it seems reasonable that the hottest dust in a galaxy could be more efficiently heated by the very energetic photons arising from the hottest (and youngest) stars than by redder photons from older stars. In contrast, the colder dust could be heated not only by the ionizing flux, but also by the emission arising from cooler (and older) stars. In such case, the luminosities in the MIR would be a better tracer of the most recent star formation than the TIR luminosity, which is dominated by the emission of colder dust (see Equations 2 and 4). This is supported by the fact that the morphologies of M81 and M51 at 24 μm resemble those of the $\text{H}\alpha$ emission (see Gordon et al. 2004 and Calzetti et al. 2005; see also Hinz et al. 2004 for M33, and Helou et al. 2004 for NGC300), which closely traces the location of the ionizing stars (in the HII regions). In contrast, the morphologies in the MIR are not as similar to the UV images, given that the UV flux is largely affected by extinction and the emission is normally linked to the star formation on a longer timescale.

We explore the possibility of using the 24 μm emission alone as a SFR tracer in Figure 8. The left panel shows the correlation between $L(24)$ and $L^{\text{corr}}(\text{H}\alpha)$ for the combined sample of HII regions in M81 and M51. The best fit to the data is:

$$\log\{L(24)\} = (-10.7 \pm 1.4) + (+1.302 \pm 0.036) \times \log\{L^{\text{corr}}(\text{H}\alpha)\} \quad (18)$$

The global scatter around this relationship is 40%. As seen in the left panel of Figure 7, the data points for M81 and M51 seem to fall on two different linear relations with very similar slopes (very close to unity) but offset (see in the inset in the left panel of Figure 8). This effect is consistent with the different $L(24)/\text{SFR}$ ratios found by Calzetti et al. (2005) for the HII regions in M51 and for entire galaxies, including starbursts and ultraluminous infrared galaxies. While the galaxies with very intense star formation show larger $L(24)/\text{SFR}$ ratios than the central region of M51, the HII regions in M81 show smaller ratios (on average, a $L(24)/\text{SFR}$ ratio a factor of three lower than the central region of M51). As pointed out by Calzetti et al. (2005), $L(24)$ alone does not seem to be a universal estimator of the total SFR of a galaxy or HII region. However, Alonso-Herrero et al. (2006) have derived an empirical relation that provides an accurate fit to the SFR (obtained from $\text{Pa}\alpha$ data) to 24 μm luminosity for the dusty M51 HII regions upward in the luminosity through $L(8 - 1000) \sim 10^{12} L_{\odot}$.

In the right panel of Figure 8, we show the alternative calibration of the 24 μm luminosity as a tracer of the amount of $\text{H}\alpha$ photons extinguished by dust, i.e., not of the total star formation, but only of the star formation which is undetectable by the observed $\text{H}\alpha$ emission due to dust extinction. The best fit to the data is:

$$\log\{L(24)\} = (+1.2 \pm 1.3) + (+1.002 \pm 0.034) \times \log\{L^{\text{abs}}(\text{H}\alpha)\} \quad (19)$$

The global scatter around this relationship is 35%. The most deviant points correspond again to the HII regions in M81 with a radio-based extinction. The slope of the fit is consistent with a value of unity, which favors a direct link between the Lyman photons (or the emission arising from the stars that dominate the production of Lyman photons) and the heating of the hottest dust in M81 and M51. Note that the SFR calculated in this way should be added to the SFR estimated from the observed emission-line to obtain the total SFR.

5.3. The 8 μm luminosity as a SFR tracer

Figure 9 shows the comparison of the 8 μm luminosity (corrected for the stellar light contamination) with the extinction corrected $\text{H}\alpha$ luminosity and the $\text{H}\alpha$ luminosity extinguished by dust. To be able to compare with our data, the 8 μm emission for the regions in M51 has been corrected for the effect of the calibration of extended sources in IRAC images (a correction of 0.133 dex). The best linear fits to the data are:

$$\log\{L(8)\} = (-4.5 \pm 1.6) + (+1.147 \pm 0.042) \times \log\{L^{\text{corr}}(\text{H}\alpha)\} \quad (20)$$

$$\log\{L(8)\} = (+5.2 \pm 1.2) + (+0.902 \pm 0.031) \times \log\{L^{\text{abs}}(\text{H}\alpha)\} \quad (21)$$

The scatter around these relations is larger than 60% in both cases. Comparing with Figures 7 and 8, Figure 9 shows that the 8 μm emission is a poorer estimator of the total or extinguished SFR than the 24 μm or TIR emissions. Within each galaxy, the data seem to follow a linear relation (with a slope that differs significantly from unity), but there are strong differences between the two galaxies. Three factors can be responsible for these differences: 1) an important residual contamination in the 8 μm fluxes from stellar emission, which might depend on the size of the apertures used and the properties of the stellar population enclosed; 2) galaxy-to-galaxy variations in the metallicity and aromatic properties and spectrum; and 3) a heterogeneous nature in the agents responsible for the excitation of the aromatic molecules that dominate the 8 μm emission (see also Calzetti et al. 2005, and references therein).

All the correlations found in this Section are summarized in Table 4.

5.4. Summary of the IR SFR tracers

All the results for M81 and M51 described in the previous subsections support the idea that the heating of the dust emitting at 24 μm (the dust at $T = 40 - 50$ K) is dominated by the light arising from the same stars that produce most of the ionizing flux, which is directly correlated with the emission-line fluxes. In addition, the spectrum around 24 μm shows a remarkable absence of any bright emission or absorption feature (such as aromatic molecules) for a wide variety of galaxies (see, e.g., Sturm et al. 2000; Armus et al. 2004; Spoon et al. 2004;

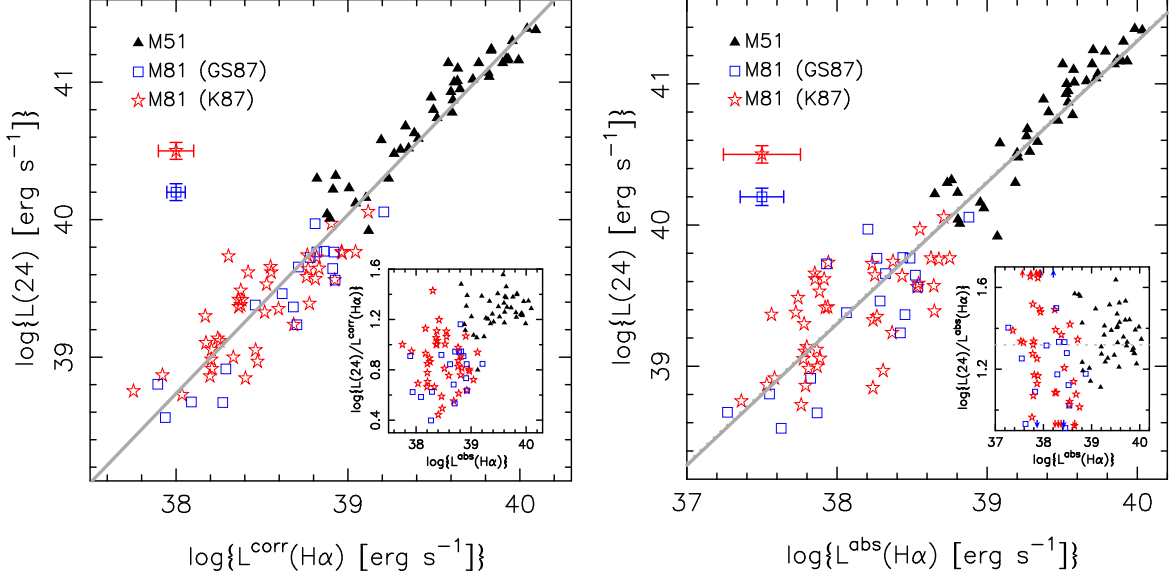


FIG. 8.— On the left, comparison between the extinction corrected $H\alpha$ and the $24\ \mu\text{m}$ luminosities for selected HII regions in M81 (with different colors and symbols referring to the distinct types of regions defined in the right panel of Figure 1, extracted from Garnett & Shields 1987 -GS87- and Kaufman et al. 1987 -K87-) and M51 (black triangles; data extracted from Calzetti et al. 2005). On the right, the $24\ \mu\text{m}$ luminosity of the same sample of HII regions is compared with the $H\alpha$ luminosity absorbed by the dust. For both panels, we show the typical uncertainties linked to each catalog of HII regions in M81. The best linear fit is plotted with a continuous gray line. The insets show the same plots but using a luminosity ratio in the vertical axis to enhance the differences in the trends followed by the datasets for each galaxy. The dotted line in the right panel (and the inset) shows the luminosity relation for slope unity.

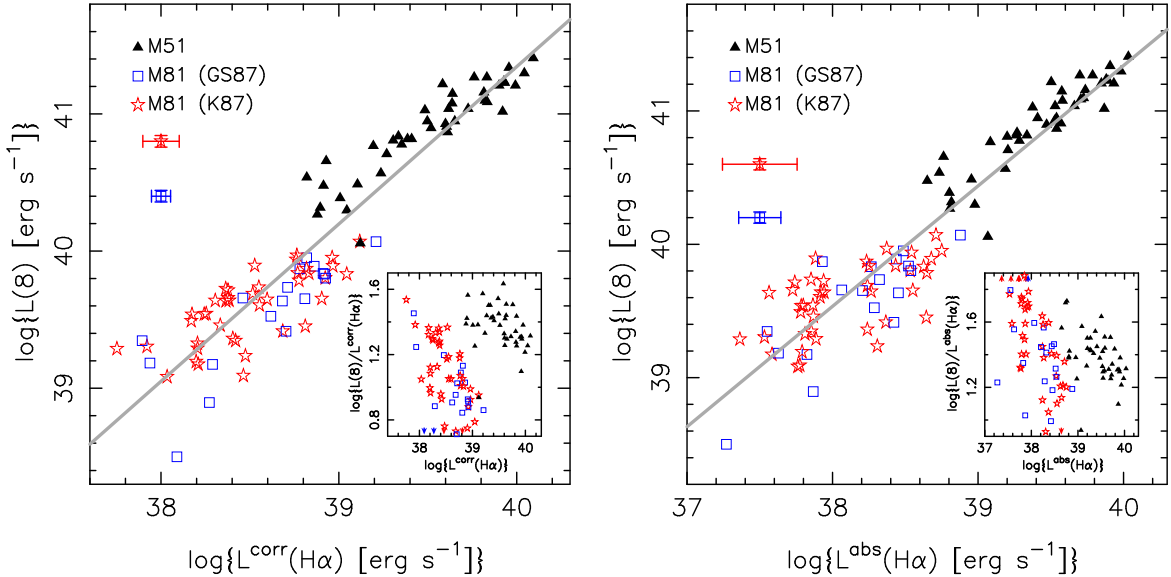


FIG. 9.— On the left, comparison between the extinction corrected $H\alpha$ and the $8\ \mu\text{m}$ luminosities for selected HII regions in M81 (with different colors and symbols referring to the distinct types of regions defined in the right panel of Figure 1, extracted from Garnett & Shields 1987 -GS87- and Kaufman et al. 1987 -K87-) and M51 (black triangles; data extracted from Calzetti et al. 2005). On the right, the $8\ \mu\text{m}$ luminosity of the same sample of HII regions is compared with the $H\alpha$ luminosity absorbed by the dust. For both panels, we show the typical uncertainties linked to each catalog of HII regions in M81. The best linear fit is plotted with a continuous gray line. The insets show the same plots but using a luminosity ratio in the vertical axis to enhance the differences in the trends followed by the datasets for each galaxy.

Smith et al. 2004; Houck et al. 2004). This means that the $24\ \mu\text{m}$ band is adequate to directly measure the continuous emission from warm dust (heated by ionizing photons) without line contaminants, in contrast to the significant contamination of other parts of the IR spectrum by aromatic emissions (e.g., 8 or $12\ \mu\text{m}$) or/and

emission from dust heated by sources not directly linked with the recent star formation (e.g., $160\ \mu\text{m}$). All these reasons support the idea that the $24\ \mu\text{m}$ emission alone is a good estimator of the obscured SFR for HII regions in a wide range of extinctions (from $A(V) \sim 0$ to $A(V) \sim 4$) and SFR (from 10^{-4} to $0.3\ \mathcal{M}_{\odot}\text{yr}^{-1}$). In the same

sense, the 8 μm emission is a poorer estimator of the SFR. But the IR luminosities alone are not directly proportional to the total SFR for HII regions in different galaxies. Regions with higher extinctions present larger SFRs (see Hopkins et al. 2001, Sullivan et al. 2001, and Pérez-González et al. 2003d) and higher IR-to- $\text{H}\alpha$ ratios that increase non-linearly with $L^{\text{corr}}(\text{H}\alpha)$. There are two reasons for this behavior: 1) the absorption of photons by dust does not scale linearly with the radiation field seen by the dust; 2) as we increase the extinction, larger zones of the HII regions become optically thick and the emission-line observations are not able to recover all the emitted flux. More data for other galaxies (spanning more extinction, SFRs, metallicities, and stellar population properties) should be added to this study to prove the universality of the correlations given in the previous subsections.

5.5. Calibration of the UV luminosity as a SFR tracer compatible with $\text{H}\alpha$ and the IR

In this Subsection, we compare the UV-derived SFRs with the $\text{H}\alpha$ observations and obtain a calibration of the UV data as a SFR tracer compatible with the $\text{H}\alpha$ emission. This calibration will allow the use of UV, $\text{H}\alpha$, and IR observations to analyze in detail the SFRs and extinction properties of HII regions.

The relationship between the luminosity in the FUV or NUV and the SFR is well known, given that the UV emission arises mainly from hot massive stars. However, the emission at these wavelengths is strongly affected by dust attenuation. This attenuation has been commonly estimated using the slope in the UV part of the spectrum. The UV slope was calibrated against the actual extinction in the UV, measured with the ratio between the IR and UV emissions, for a sample of starburst galaxies by Meurer et al. (1999). This calibration has been extensively used in the literature, but several studies have shown that the relationship found for starbursts cannot be applied to all galaxies (see, e.g., Bell 2002; Kong et al. 2004; Buat et al. 2005). Star-forming regions in M81 (Gordon et al. 2004) and M51 (Calzetti et al. 2005) have also been shown to depart significantly from the starburst relationship. All these works have shown that the relationship between the UV slope and the extinction depends on factors such as the age of the stellar population, the metallicity and the attenuation law (which depends on the dust properties and the dust-stars geometry). The difficulties in extinction correction prevent the use of the UV emission alone as an accurate SFR tracer.

Another possibility is to use the UV emission to estimate the SFR not obscured by dust, and to add this component to the obscured SFR estimated with the IR emission. This method is similar to the one used in Bell (2003). It is also analogous to the procedure we followed in the previous subsections, where we showed the good correlation between the 24 μm luminosity and the SFR that is obscured by dust and cannot be detected with an emission-line such as $\text{H}\alpha$ or $\text{Pa}\alpha$. The narrow-band data for those lines are very expensive to obtain in terms of observing time. Therefore, it would be convenient to have an estimate of the SFR not hidden by dust using other observations which were relatively easier to obtain, such as the GALEX UV data. The goal is to translate the broad-band UV emission to an integrated emission in

the UV, and that to a non-obscured SFR consistent with the ionized hydrogen emission. In principle, the $\text{H}\alpha$ emission traces a stellar population with a shorter timescale than the UV (about 10 Myr for $\text{H}\alpha$ and 100 Myr for the UV), given that the emission-line is linked to the hottest (and youngest) stars dominating the production of ionizing photons. The $\text{H}\alpha$ /UV ratio should be more and more independent of the star formation history of the galaxy as we move to shorter wavelengths in the UV (Buat et al. 2002; Bell 2002). The extinction also plays an important role, since it affects the stellar and ionized gas emission differently (see, e.g., Calzetti et al. 2000; Charlot & Fall 2000; Bell et al. 2002).

In Figure 10, we plot the relationships between the observed $\text{H}\alpha$ emission and the luminosities in the two GALEX UV bands for the HII regions in M81 and the central part of M51. The left panel shows that the NUV luminosity is not directly proportional to the $\text{H}\alpha$ emission (a proportionality would show in the figure as a cloud of points around an average value, but there is an offset between the M51 and M81 points). The lack of correlation is related to the fact that the NUV emission arises from cooler stars than the ones that dominate the production of ionizing photons (i.e., the difference in the timescales of the star formation traced by $\text{H}\alpha$ and the NUV is relatively large). The different luminosity ratio found for M81 and M51 should also be related to the larger (extinction corrected) SFRs observed for the regions in M51. The correlation between the FUV and $\text{H}\alpha$ emission is considerably better (i.e., they are roughly proportional), although there still seems to be an offset between the M81 and M51 data. This panel shows that the FUV luminosity probes a stellar population that is closer to that producing the Lyman photons, as expected.

The first two panels of Figure 10 show that there is not a direct correlation between the broad-band UV emission and the observed $\text{H}\alpha$ luminosity, since parameters such as the age of the stellar population and the extinction affect both quantities in differing amounts. In the last panel of Figure 10, we explore the possibility of using the two GALEX luminosities to obtain an estimation of the unobscured SFR consistent with the observed $\text{H}\alpha$ emission. For this purpose, we obtained a relationship between the observed $\text{H}\alpha$ luminosity and the emission in the two UV bands using a singular value decomposition method. By using the two UV fluxes, the relation is intended to cope with the two parameters affecting the UV slope, the age and the extinction (for a fixed metallicity), and to allow obtaining an estimate of the unobscured SFR from UV data consistent with the observed $\text{H}\alpha$ flux. The result is the following:

$$\log\{L(\text{H}\alpha)\} = +1.437 \times \log\{L(\text{FUV})\} + (-0.478) \times \log\{L(\text{NUV})\} \equiv \log\{L(\text{GALEX})\} \quad (22)$$

This empirical relationship allows estimating the unobscured SFR using the GALEX data with a scatter of 40%. More data for other galaxies should be added to this study to prove the universality and usefulness of such a correlation.

5.6. The radial trend in the dust attenuation

Figure 11 shows a radial plot of the ratio between the obscured SFR (calculated with the 24 μm luminosity,

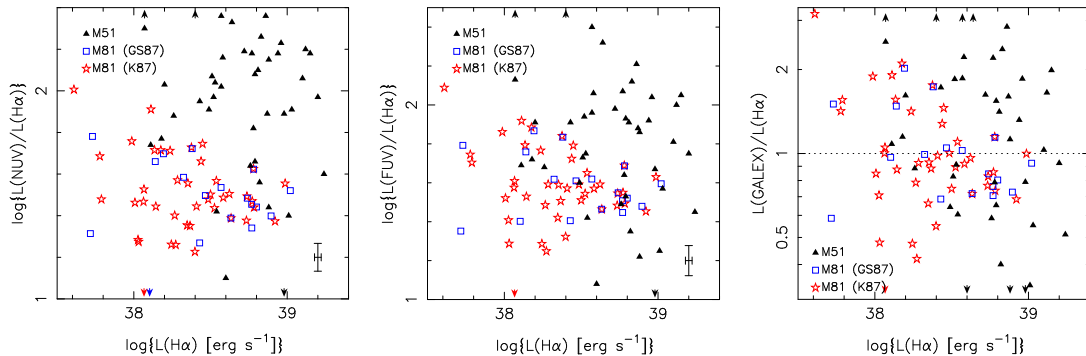


FIG. 10.— In the first two panels, we show the comparison between the observed luminosities in the two GALEX UV bands and the observed $H\alpha$ emission. In the right panel, we compare the observed $H\alpha$ emission with a combined UV luminosity obtained with the two GALEX bands, $L(GALEX)$ (defined in Equation 22), built to match the observed $H\alpha$ emission. In this panel, the expected luminosity ratio of unity (if $L(GALEX)$ and $L(H\alpha)$ match perfectly) is also shown.

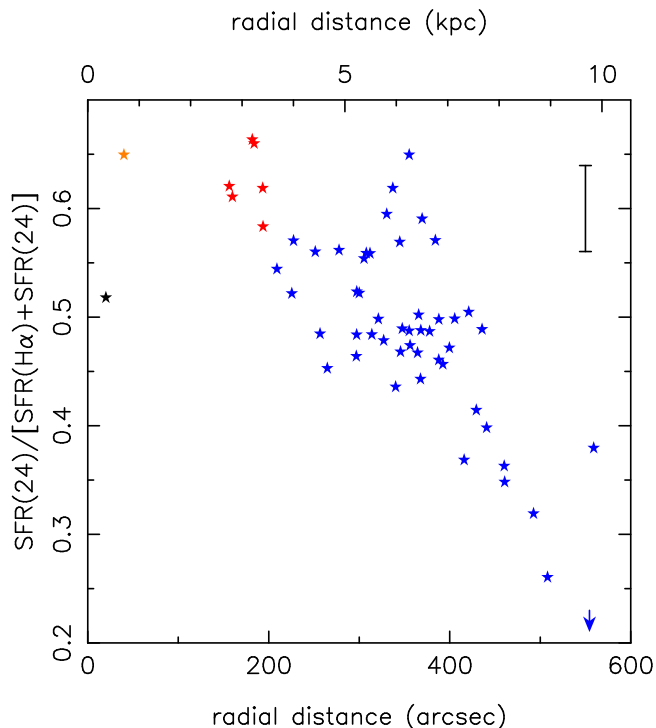


FIG. 11.— Radial dependence (de-projected) of the ratio between the obscured SFR estimated from the $24\ \mu\text{m}$ luminosity (using the calibration in Equation 19) and the total SFR calculated with the observed $H\alpha$ and $24\ \mu\text{m}$ emissions. The different colors refer to the distinct types of regions defined in Figure 1. The average surface density of the entire galaxy has been plotted at $r = 20''$, and the surface density for the nuclear and the circumnuclear regions has been plotted at $r = 40''$ (slightly shifted from $r = 0$ for clarity).

translated to an equivalent absorbed $H\alpha$ luminosity with Equation 19, and from that to a SFR using the calibration in Kennicutt 1998) and the total SFR (calculated as the sum of the unobscured and obscured SFRs with the observed $H\alpha$ and $24\ \mu\text{m}$ emissions) for the regions defined in the 160RES image set¹⁸ and using the LOCAL-BKG photometry. There is a clear gradient in the SFR

¹⁸ We have used the 160RES regions because they span a wider range of radial distances than the 24RES regions

ratio, i.e., there is a decrease in the extinction of the stellar light as we move away from the center of the galaxy. This gradient is consistent with the results we found in Section 4 about the radial trend in two other quantities: the dust temperature and the dust mass surface density. It is also consistent with results obtained for M81 and other galaxies in the literature (Boissier et al. 2004; Holwerda et al. 2005; Roussel et al. 2005; Prescott et al. 2006).

Figure 11 also shows that for the entire M81 galaxy, the IR just sees $\sim 50\%$ of the total SFR; the other 50% is linked with star formation that is not obscured by dust. The largest percentages are observed for the regions dominated by very diffuse emission, where about 65% of the star formation is seen in the IR. For the most remote regions in the disk, the IR alone can miss up to $\sim 80\%$ of the star formation. The gradient in the SFR ratio implies a radial change in the $H\alpha$ extinction from $A(H\alpha) \sim 1.0$ to $A(H\alpha) \sim 0.2$ along the disk of M81, the observed range for the 24RES regions used in the previous subsections.

6. SUMMARY AND CONCLUSIONS

The recent star formation in the early-type spiral galaxy M81 has been analyzed in two dimensions using imaging observations spanning the electromagnetic spectrum from the far ultraviolet (UV) to the far infrared (IR). The data have been compared to models of stellar, gas, and dust emission, obtaining results for different sub-galactic regions whose sizes range from those typical of individual HII regions ($0.1\ \text{kpc}$) to the sizes of dynamical structures ($2\ \text{kpc}$).

The main results of this work are:

- 1.- Using stellar population models, we confirm that the luminosities in the mid-IR bands (from 3 to $8\ \mu\text{m}$) contain substantial contributions from both dust and stellar light. These contributions vary significantly depending on the spatial resolution and environment, suggesting the existence of mid- and far-IR diffuse dust emission not directly linked to the recent star formation.
- 2.- The IR emission of M81 can be modeled with three components: 1) a cold dust component of average temperature $T_c = 18 \pm 2\ \text{K}$; 2) a warm compo-

TABLE 4
SUMMARY OF CORRELATIONS BETWEEN DIFFERENT SFR ESTIMATORS.

Estimator	$\log [L^{\text{corr}}(\text{H}\alpha)]$			$\log [L^{\text{abs}}(\text{H}\alpha)]$		
	a	b	σ	a	b	σ
$\log [L(8 - 1000)]$	2.3±1.2	0.992±0.031	30%	8.9±1.0	0.826±0.025	30%
$\log [L(24)]$	-10.7±1.4	1.302±0.036	40%	1.2±1.3	1.002±0.034	30%
$\log [L(8)]$	-4.5±1.6	1.147±0.042	60%	5.2±1.2	0.902±0.031	60%

NOTE. — The Table shows the coefficients of the correlations between the luminosity given in the first column and $\log L^{\text{corr}}(\text{H}\alpha)$ or $\log L^{\text{abs}}(\text{H}\alpha)$. The equation for the correlation is: $\log [L(\lambda)] = a + b \times \log [L^?(\text{H}\alpha)]$. In the fourth and seventh columns of the Table, σ is the scatter around the linear relation. All luminosities are given in erg s^{-1} .

ment with $T_w = 53 \pm 7$ K; and 3) polycyclic aromatic molecules with different properties. While the emission of the hotter dust (peaking at around $24 \mu\text{m}$) is very concentrated in the HII regions, the emission of the colder dust component (peaking near $160 \mu\text{m}$) and the aromatic molecules (contributing importantly to the $8 \mu\text{m}$ emission) show a more diffuse distribution. This suggests the presence of an alternative heating source different than the stars recently formed in the HII regions (older stars in the disk), or the importance of the transfer of energy (e.g., the ionizing flux) from the HII regions to the interstellar medium (i.e., the escape of photons from the HII regions that interact with dust in distant zones of the disk).

- 3.- A negative radial gradient is observed in the dust temperature of the cold dust component, the dust mass surface density (similar to the gradient of the molecular gas surface density found by Devereux et al. 1995), and the comparison between the star formation rate (SFR) indicators affected by dust extinction (*UV* and $\text{H}\alpha$ emission) and the IR emission (see also Roussel et al. 2005; Prescott et al. 2006).
- 4.- For the entire M81 galaxy, about 50% of the star formation is obscured by dust and can be seen in the IR, and the other half can be traced directly with the observed $\text{H}\alpha$ emission. The percentage of obscured star formation ranges from 60% in the inner regions of the galaxy to 30% in the most distant zones.
- 5.- Based on our dust emission models, we have built several empirical relations between the monochromatic fluxes in the IR and the total IR emission [integrated between 8 and $1000 \mu\text{m}$, $L(8 - 1000)$], useful for sub-galactic regions in spiral galaxies with $10^7 \lesssim L(8 - 1000) \lesssim 10^8 L_\odot$. These correlations differ significantly from the ones found in the literature for entire IR-bright galaxies, mainly because of the presence of a colder dust component.
- 6.- We have compared five different SFR estimators for individual HII regions in M81 and M51: the UV, the $\text{H}\alpha$ emission, and three estimators based on *Spitzer* IR data. Several empirical relations have

been built to estimate the total SFR of HII regions from IR data alone, or from a combination of IR fluxes (which account for the obscured star formation) and UV/optical data (directly measuring the unobscured star formation). The typical scatter of data around these relations is 30-50%, with possible important additional variations of the correlations from galaxy to galaxy.

- 7.- Among the SFR estimators in the IR, the $24 \mu\text{m}$ emission has the best correlation with the $\text{H}\alpha$ luminosity extinguished by dust. The correlation is worse for the total IR luminosity, which suggests that the colder dust dominating the total IR luminosity is (also) heated by redder photons. The $8 \mu\text{m}$ luminosity is not directly correlated with the ionized gas emission, making it in an unreliable SFR estimator. These results are consistent with those found in Calzetti et al. (2005) and Kennicutt et al. (2006).
- 8.- Important variations from galaxy to galaxy are found when estimating the total SFR with the $24 \mu\text{m}$ or the total IR emission alone. We suggest the combination of the $\text{H}\alpha$ (or the UV) and an IR luminosity (especially the rest-frame $24 \mu\text{m}$ emission, calibrated in Kennicutt et al. 2006 and in this paper with the M81 and M51 data) to obtain the most reliable estimates of the total SFRs for HII regions (and, by extrapolation, for galaxies). Those emissions probe the unobscured and obscured star formation, respectively.
- 9.- Additional data for other galaxies (spanning more extinction, SFRs, metallicities, and stellar population properties) should be added to this study to prove the universality of the correlations found in this paper.

We thank an anonymous referee for her/his useful comments. Support for this work was provided by NASA through Contract no. 1255094 issued by JPL/Caltech. This work is part of SINGS, the Spitzer Infrared Nearby Galaxies Survey, one of the Spitzer Space Telescope Legacy Science Programs, and was supported by the JPL, Caltech, contract 1224667. This work is based in

part on observations made with the *Spitzer* Space Telescope, which is operated by the Jet Propulsion Laboratory, Caltech under NASA contract 1407. GALEX is a NASA Small Explorer launched in 2003 April. We gratefully acknowledge NASA's support for construction, operation, and scientific analysis of the GALEX mission. This research has made use of the NASA/IPAC Extra-

galactic Database (NED) which is operated by the Jet Propulsion Laboratory, California Institute of Technology, under contract with the National Aeronautics and Space Administration. P.G. P.-G. and A. G. de P. also wish to acknowledge support from the Spanish Programa Nacional de Astronomía y Astrofísica under grant AYA 2004-01676.

REFERENCES

- Allamandola, L. J., Tielens, A. G. G. M., & Barker, J. R. 1985, *ApJ*, 290, L25
- Alonso-Herrero et al. 2006, *ApJ* (in press)
- Armus, L. et al. 2004, *ApJS*, 154, 178
- Bell, E. F. 2002, *ApJ*, 577, 150
- . 2003, *ApJ*, 586, 794
- Bell, E. F., & de Jong, R. S. 2001, *ApJ*, 550, 212
- Bell, E. F., Gordon, K. D., Kennicutt, R. C., & Zaritsky, D. 2002, *ApJ*, 565, 994
- Bendo, G. J. et al. 2003, *AJ*, 125, 2361
- Boissier, S., Boselli, A., Buat, V., Donas, J., & Milliard, B. 2004, *A&A*, 424, 465
- Boselli, A., Lequeux, J., & Gavazzi, G. 2004, *A&A*, 428, 409
- Brinchmann, J., Charlot, S., White, S. D. M., Tremonti, C., Kauffmann, G., Heckman, T., & Brinkmann, J. 2004, *MNRAS*, 351, 1151
- Brocklehurst, M. 1971, *MNRAS*, 153, 471
- Brouillet, N., Baudry, A., Combes, F., Kaufman, M., & Bash, F. 1991, *A&A*, 242, 35
- Buat, V., Boselli, A., Gavazzi, G., & Bonfanti, C. 2002, *A&A*, 383, 801
- Buat, V. et al. 2005, *ApJ*, 619, L51
- Calzetti, D. 2001, *PASP*, 113, 1449
- Calzetti, D., Armus, L., Bohlin, R. C., Kinney, A. L., Koornneef, J., & Storchi-Bergmann, T. 2000, *ApJ*, 533, 682
- Calzetti, D. et al. 2005, *ApJ*, 633, 871
- Cardelli, J. A., Clayton, G. C., & Mathis, J. S. 1989, *ApJ*, 345, 245
- Charlot, S., & Fall, S. M. 2000, *ApJ*, 539, 718
- Chary, R., & Elbaz, D. 2001, *ApJ*, 556, 562
- Code, A. D., & Welch, G. A. 1982, *ApJ*, 256, 1
- Condon, J. J. 1992, *ARA&A*, 30, 575
- Conselice, C. J., Gallagher, J. S., Calzetti, D., Homeier, N., & Kinney, A. 2000, *AJ*, 119, 79
- Dale, D. A. et al. 2005, *ApJ*, 633, 857
- Dale, D. A., & Helou, G. 2002, *ApJ*, 576, 159
- de Vaucouleurs, G., de Vaucouleurs, A., Corwin, H. G., Buta, R. J., Paturel, G., & Fouque, P. 1992, *VizieR Online Data Catalog*, 7137, 0
- Devereux, N. A., Jacoby, G., & Ciardullo, R. 1995, *AJ*, 110, 1115
- Devriendt, J. E. G., Guiderdoni, B., & Sadat, R. 1999, *A&A*, 350, 381
- Draine et al. 2006, *ApJ* (in preparation)
- Dunne, L., Eales, S., Edmunds, M., Ivison, R., Alexander, P., & Clements, D. L. 2000, *MNRAS*, 315, 115
- Dunne, L., & Eales, S. A. 2001, *MNRAS*, 327, 697
- Elvis, M., & van Speybroeck, L. 1982, *ApJ*, 257, L51
- Engelbracht, C. W. et al. 2004, *ApJS*, 154, 248
- Engelbracht, C. W., Gordon, K. D., Rieke, G. H., Werner, M. W., Dale, D. A., & Latter, W. B. 2005, *ApJ*, 628, L29
- Fabbiano, G. 1988, *ApJ*, 325, 544
- Fazio, G. G. et al. 2004, *ApJS*, 154, 10
- Ferland, G. J. 1980, *PASP*, 92, 596
- Filippenko, A. V., & Sargent, W. L. W. 1988, *ApJ*, 324, 134
- Fioc, M., & Rocca-Volmerange, B. 1997, *A&A*, 326, 950
- Flores, H. et al. 1999, *ApJ*, 517, 148
- Förster Schreiber, N. M., Roussel, H., Sauvage, M., & Charmandaris, V. 2004, *A&A*, 419, 501
- Franceschini, A., Aussel, H., Cesarsky, C. J., Elbaz, D., & Fadda, D. 2001, *A&A*, 378, 1
- Freedman, W. L. et al. 1994, *ApJ*, 427, 628
- Garnett, D. R., & Shields, G. A. 1987, *ApJ*, 317, 82
- Genzel, R., & Cesarsky, C. J. 2000, *ARA&A*, 38, 761
- Gil de Paz, A., Aragón-Salamanca, A., Gallego, J., Alonso-Herrero, A., Zamorano, J., & Kauffmann, G. 2000, *MNRAS*, 316, 357
- Gil de Paz, A., & Madore, B. F. 2002, *AJ*, 123, 1864
- Goldader, J. D., Meurer, G., Heckman, T. M., Seibert, M., Sanders, D. B., Calzetti, D., & Steidel, C. C. 2002, *ApJ*, 568, 651
- Gordon, K. D., Clayton, G. C., Witt, A. N., & Misselt, K. A. 2000, *ApJ*, 533, 236
- Gordon, K. D. et al. 2004, *ApJS*, 154, 215
- . 2005, *PASP*, 117, 503
- Gordon et al. 2006, *ApJ* (submitted)
- Gottesman, S. T., & Weliachew, L. 1975, *ApJ*, 195, 23
- Greenawalt, B., Walterbos, R. A. M., Thilker, D., & Hoopes, C. G. 1998, *ApJ*, 506, 135
- Heavens, A., Panter, B., Jimenez, R., & Dunlop, J. 2004, *Nature*, 428, 625
- Heckman, T. M. 1980, *A&A*, 87, 152
- Helou, G. et al. 2004, *ApJS*, 154, 253
- Hill, J. K. et al. 1992, *ApJ*, 395, L37
- . 1995, *ApJ*, 438, 181
- Hinz, J. L. et al. 2004, *ApJS*, 154, 259
- Hippelein, H., Haas, M., Tuffs, R. J., Lemke, D., Stickel, M., Klaas, U., & Völk, H. J. 2003, *A&A*, 407, 137
- Ho, L. C., Filippenko, A. V., & Sargent, W. L. W. 1997, *ApJS*, 112, 315
- Høg, E. et al. 2000, *A&A*, 357, 367
- Holwerda, B. W., González, R. A., van der Kruit, P. C., & Allen, R. J. 2005, *A&A*, 444, 109
- Hopkins, A. M. 2004, *ApJ*, 615, 209
- Hopkins, A. M., Connolly, A. J., Haarsma, D. B., & Cram, L. E. 2001, *AJ*, 122, 288
- Houck, J. R. et al. 2004, *ApJS*, 154, 211
- Jarrett, T. H., Chester, T., Cutri, R., Schneider, S., Skrutskie, M., & Huchra, J. P. 2000, *AJ*, 119, 2498
- Karachentsev, I. D. et al. 2002, *A&A*, 383, 125
- Kauffmann, G. et al. 2003, *MNRAS*, 341, 33
- Kaufman, M., Bash, F. N., Kennicutt, R. C., & Hodge, P. W. 1987, *ApJ*, 319, 61
- Kennicutt, R. C. 1998, *ARA&A*, 36, 189
- Kennicutt, R. C. et al. 2003, *PASP*, 115, 928
- Kennicutt et al. 2006, *ApJ* (in press)
- Kewley, L. J., Geller, M. J., Jansen, R. A., & Dopita, M. A. 2002, *AJ*, 124, 3135
- Kleinmann, D. E., & Low, F. J. 1970, *ApJ*, 161, L203
- Kong, X., Charlot, S., Brinchmann, J., & Fall, S. M. 2004, *MNRAS*, 349, 769
- Kong, X. et al. 2000, *AJ*, 119, 2745
- La Parola, V., Fabbiano, G., Elvis, M., Nicastro, F., Kim, D. W., & Peres, G. 2004, *ApJ*, 601, 831
- Laor, A., & Draine, B. T. 1993, *ApJ*, 402, 441
- Leger, A., & Puget, J. L. 1984, *A&A*, 137, L5
- Li, A., & Draine, B. T. 2001, *ApJ*, 554, 778
- Lin, W. et al. 2003, *AJ*, 126, 1286
- Martin, D. C. et al. 2005, *ApJ*, 619, L1
- Meurer, G. R., Heckman, T. M., & Calzetti, D. 1999, *ApJ*, 521, 64
- Morrissey, P. et al. 2005, *ApJ*, 619, L7
- Osterbrock, D. E. 1989, *Astrophysics of gaseous nebulae and active galactic nuclei* (Research supported by the University of California, John Simon Guggenheim Memorial Foundation, University of Minnesota, et al. Mill Valley, CA, University Science Books, 1989, 422 p.)
- Pérez-González, P. G., Gallego, J., Zamorano, J., Alonso-Herrero, A., de Paz, A. G., & Aragón-Salamanca, A. 2003a, *ApJ*, 587, L27
- Pérez-González, P. G., Gil de Paz, A., Zamorano, J., Gallego, J., Alonso-Herrero, A., & Aragón-Salamanca, A. 2003b, *MNRAS*, 338, 508
- . 2003c, *MNRAS*, 338, 525
- Pérez-González, P. G. et al. 2005, *ApJ*, 630, 82
- Pérez-González, P. G., Zamorano, J., Gallego, J., Aragón-Salamanca, A., & Gil de Paz, A. 2003d, *ApJ*, 591, 827

- Page, M. J., Breeveld, A. A., Soria, R., Wu, K., Branduardi-Raymont, G., Mason, K. O., Starling, R. L. C., & Zane, S. 2003, *A&A*, 400, 145
- Pahre, M. A., Ashby, M. L. N., Fazio, G. G., & Willner, S. P. 2004, *ApJS*, 154, 235
- Papovich, C., Dickinson, M., & Ferguson, H. C. 2001, *ApJ*, 559, 620
- Peeters, E., Spoon, H. W. W., & Tielens, A. G. G. M. 2004, *ApJ*, 613, 986
- Peimbert, M., & Torres-Peimbert, S. 1981, *ApJ*, 245, 845
- Petre, R., Mushotzky, R. F., Serlemitsos, P. J., Jahoda, K., & Marshall, F. E. 1993, *ApJ*, 418, 644
- Popescu, C. C., & Tuffs, R. J. 2003, *A&A*, 410, L21
- Popescu, C. C. et al. 2005, *ApJ*, 619, L75
- Popescu, C. C., Tuffs, R. J., Völk, H. J., Pierini, D., & Madore, B. F. 2002, *ApJ*, 567, 221
- Prescott et al. 2006, *ApJ* (in press)
- Puget, J. L., & Leger, A. 1989, *ARA&A*, 27, 161
- Reach, W. T. et al. 2005, *PASP*, 117, 978
- Regan, M. W. et al. 2004, *ApJS*, 154, 204
- Reichen, M., Kaufman, M., Blecha, A., Golay, M., & Huguenin, D. 1994, *A&AS*, 106, 523
- Rice, W., Lonsdale, C. J., Soifer, B. T., Neugebauer, G., Koplan, E. L., Lloyd, L. A., de Jong, T., & Habing, H. J. 1988, *ApJS*, 68, 91
- Rieke, G. H., & Low, F. J. 1972, *ApJ*, 176, L95
- Rieke, G. H. et al. 2004, *ApJS*, 154, 25
- Rots, A. H., & Shane, W. W. 1975, *A&A*, 45, 25
- Roussel, H., Gil de Paz, A., Seibert, M., Helou, G., Madore, B. F., & Martin, C. 2005, *ApJ*, 632, 227
- Rowan-Robinson, M. 2001, *ApJ*, 549, 745
- Sage, L. J., & Westpfahl, D. J. 1991, *A&A*, 242, 371
- Sanders, D. B., & Mirabel, I. F. 1996, *ARA&A*, 34, 749
- Saunders, W., Rowan-Robinson, M., Lawrence, A., Efstathiou, G., Kaiser, N., Ellis, R. S., & Frenk, C. S. 1990, *MNRAS*, 242, 318
- Sauvage, M., & Thuan, T. X. 1992, *ApJ*, 396, L69
- Schlegel, D. J., Finkbeiner, D. P., & Davis, M. 1998, *ApJ*, 500, 525
- Shuder, J. M., & Osterbrock, D. E. 1981, *ApJ*, 250, 55
- Smith, J. D. T. et al. 2004, *ApJS*, 154, 199
- Solinger, A., Morrison, P., & Markert, T. 1977, *ApJ*, 211, 707
- Spoon, H. W. W. et al. 2004, *ApJS*, 154, 184
- Stauffer, J. R., & Bothun, G. D. 1984, *AJ*, 89, 1702
- Stickel, M., Barnes, D., & Krause, O. 2005, *A&A*, 443, 373
- Sturm, E., Lutz, D., Tran, D., Feuchtgruber, H., Genzel, R., Kunze, D., Moorwood, A. F. M., & Thornley, M. D. 2000, *A&A*, 358, 481
- Sullivan, M., Mobasher, B., Chan, B., Cram, L., Ellis, R., Treyer, M., & Hopkins, A. 2001, *ApJ*, 558, 72
- Walterbos, R. A. M., & Greenawalt, B. 1996, *ApJ*, 460, 696
- Weingartner, J. C., & Draine, B. T. 2001, *ApJ*, 548, 296
- Werner, M. W. et al. 2004a, *ApJS*, 154, 1
- Werner, M. W., Uchida, K. I., Sellgren, K., Marengo, M., Gordon, K. D., Morris, P. W., Houck, J. R., & Stansberry, J. A. 2004b, *ApJS*, 154, 309
- Williams, G. G., Olszewski, E., Lesser, M. P., & Burge, J. H. 2004, in *Ground-based Instrumentation for Astronomy*. Edited by Alan F. M. Moorwood and Iye Masanori. *Proceedings of the SPIE*, Volume 5492, pp. 787-798 (2004), 787-798
- Witt, A. N., & Gordon, K. D. 2000, *ApJ*, 528, 799
- Worthey, G. 1994, *ApJS*, 95, 107
- Wu, C.-C., Gallagher, J. S., Peck, M., Faber, S. M., & Tinsley, B. M. 1980, *ApJ*, 237, 290
- Youngblood, A. J., & Hunter, D. A. 1999, *ApJ*, 519, 55
- Zaritsky, D., Kennicutt, R. C., & Huchra, J. P. 1994, *ApJ*, 420, 87